



This is a repository copy of *Post-tectonic landscape evolution in NE Iberia using staircase terraces: Combined effects of uplift and climate*.

White Rose Research Online URL for this paper:
<http://eprints.whiterose.ac.uk/117580/>

Version: Accepted Version

Article:

Lewis, C.J., Sancho, C., McDonald, E.V. et al. (5 more authors) (2017) Post-tectonic landscape evolution in NE Iberia using staircase terraces: Combined effects of uplift and climate. *Geomorphology*, 292. pp. 85-103. ISSN 0169-555X

<https://doi.org/10.1016/j.geomorph.2017.04.037>

Article available under the terms of the CC-BY-NC-ND licence
(<https://creativecommons.org/licenses/by-nc-nd/4.0/>)

Reuse

Items deposited in White Rose Research Online are protected by copyright, with all rights reserved unless indicated otherwise. They may be downloaded and/or printed for private study, or other acts as permitted by national copyright laws. The publisher or other rights holders may allow further reproduction and re-use of the full text version. This is indicated by the licence information on the White Rose Research Online record for the item.

Takedown

If you consider content in White Rose Research Online to be in breach of UK law, please notify us by emailing eprints@whiterose.ac.uk including the URL of the record and the reason for the withdrawal request.

1
2
3
4 1 **Post-tectonic landscape evolution in NE Iberia using staircase terraces:**
5
6 2 **combined effects of uplift and climate**
7
8

9
10 3 Claudia J. Lewis¹, Carlos Sancho^{2*}, Eric V. McDonald³, José Luis Peña-Monné⁴, Emilio L.
11
12 4 Pueyo^{5,6}, Edward Rhodes⁷, Mikel Calle⁸, Ruth Soto^{5,6}
13
14

15 5 ¹ Earth and Environmental Sciences Division, Los Alamos National Laboratory, 87545
16
17 6 Los Alamos, NM, USA
18
19

20
21 7 ² Ciencias de la Tierra, Universidad de Zaragoza, Pedro Cerbuna 12, 50009 Zaragoza,
22
23 8 Spain
24
25

26 9 ³ Desert Research Institute, 2215 Raggio Parkway, Reno, NV, USA
27
28
29

30 10 ⁴ Geografía y Ordenación del Territorio, Universidad de Zaragoza, Pedro Cerbuna 12,
31
32 11 50009 Zaragoza, Spain
33
34

35 12 ⁵ Instituto Geológico y Minero de España, Unidad de Zaragoza, Manuel Lasala 44,
36
37 13 50006 Zaragoza, Spain
38
39

40
41 14 ⁶ Unidad Asociada en Ciencias de la Tierra IGME-Universidad de Zaragoza
42
43

44 15 ⁷ Department of Geography, The University of Sheffield, Sheffield S10 2TN, UK
45
46

47 16 ⁸ Museo Nacional de Ciencias Naturales, CSIC, José Gutiérrez Abascal 2, 28006 Madrid,
48
49 17 Spain
50

51
52
53 18 *** Corresponding author:**
54
55
56
57
58
59

60
61
62 19 Carlos Sancho Marcén
63
64 20 Departamento de Ciencias de la Tierra
65
66
67 21 Universidad de Zaragoza
68
69 22 Pedro Cerbuna, 12
70
71 23 50009 Zaragoza
72
73
74 24 Spain
75
76 25 Email: csancho@unizar.es
77
78 26 Phone: +34976761091
79
80
81 27
82
83
84
85 28
86
87
88 29
89
90
91 30
92
93
94
95 31
96
97
98 32
99
100
101 33
102
103
104
105 34
106
107
108 35
109
110
111 36
112
113
114
115 37
116
117
118

119
120
121 **Abstract**
122

123
124 39 River incision into bedrock resulting from the combined effects of tectonic uplift and
125
126
127 40 climate governs long-term regional landscape evolution. We determined spatial and
128
129 41 temporal patterns of post-orogenic stream incision from a sequence of well-preserved
130
131 42 staircase terraces developed over the last 1 Ma in the Central Pyrenees and its
132
133 43 southern foreland Ebro basin (NE Spain). Extensive remnants of ten vertically
134
135
136 44 separated terraces (Qt1 to Qt10, from oldest to youngest) were mapped along 170 km
137
138 45 of the Cinca River valley, transverse to the Pyrenean mountain belt. Multiple outcrops
139
140 46 appear in the upper reach of the valley (Ainsa sector, 50 km from headwaters) as well
141
142
143 47 as in the lower reach (Albalate sector, 125 km from headwaters). Fluvial incision into
144
145 48 bedrock was calculated using (i) differentially corrected GPS measurements of the
146
147 49 altitude of straths and (ii) numerical dating of alluvial sediments from the lower
148
149 50 terraces (Qt5 to Qt9) by Optically Stimulated Luminescence, previously reported by
150
151
152 51 Lewis et al. (2009), and supplemented with new dates for the upper terraces (Qt1, Qt2
153
154 52 and Qt3) based on palaeomagnetism and supported by soil development. Considering
155
156 53 altitude differences and the elapsed time between successive well preserved terrace
157
158 54 couples (Qt3-Qt7, Qt7-Qt9 and Qt9-Active channel), mean bedrock incision rates
159
160
161 55 ranged from 0.76 to 0.38 m ka⁻¹, at the upper reach of the valley (Ainsa section), and
162
163 56 from 0.61 to 0.20 m ka⁻¹, at the lower reach (Albalate section). River incision along the
164
165 57 valley produced vertically separated, near-parallel longitudinal terrace profiles
166
167
168 58 evidencing a rapid near-uniform regional uplift as response to (i) the tectonic
169
170 59 lithospheric thickening in NE Iberia and (ii) the erosional download rebound related to
171
172 60 the Ebro basin exorheism. Moreover, a subtle upstream divergence of strath profiles
173
174
175
176
177

178
179
180 61 may have been a consequence of an increase in uplift rate toward the head of the
181
182 62 valley. Additionally, incision rates changed over time as indicate results from the lower
183
184
185 63 reach (Albalate section); the maximum rate was 1.48 m ka^{-1} between Qt7 (61 ka) and
186
187 64 Qt8 (47 ka), and the minimum rate was 0.11 m ka^{-1} between Qt3 (401 ka) and Qt5 (178
188
189 65 ka). The highest incision rates were produced after the Marine Isotope Stage 4 most
190
191 66 likely in response to (i) an increased snowmelt discharge during the subsequent
192
193 67 deglaciation related to the last maximum advance of glaciers in the southern Pyrenees,
194
195
196 68 and (ii) a limited width of the valley after Qt7 formation, resulting from the
197
198 69 deactivation of the westward river migration. Therefore, incision rates over the last 1
199
200
201 70 Ma in the Cinca River valley were basically controlled by near-uniform bedrock uplift,
202
203 71 in the context of climate variability. The results reported in this study represent
204
205 72 significant data on fluvial incision in NE Iberia, and provide an assessment of the
206
207 73 regional post-tectonic landscape evolution.

208
209
210
211 74 **Key words:** Fluvial incision, Staircase terraces, Uplift, Climate change, Mid- to Late
212
213 75 Pleistocene, Southern Pyrenees and Ebro Basin

237
238
239 **82 1. Introduction**
240
241

242 83 Landscape evolution represents a morphotopographic balance resulting from
243
244
245 84 interactive competition between tectonics, climate and denudation processes (e.g.,
246
247 85 Burbank and Anderson, 2001; Willet et al., 2006; Cloetingh and Willett, 2013). Fluvial
248
249 86 terraces are excellent geomorphic markers that have been used extensively to
250
251
252 87 document landscape evolution (e.g., Bridgland and Westaway, 2008; Westaway et al.,
253
254 88 2009). Long-term geomorphic configuration of fluvial systems involves the
255
256 89 entrenchment of river valleys and the creation of staircase terrace sequences in
257
258
259 90 response to the basic driving forces of regional climate, tectonic uplift and base level
260
261 91 (e.g., Bridgland, 2000; Starkel, 2003; Gibbard and Lewin, 2009; Westaway et al., 2009;
262
263 92 Stokes et al., 2012; Pazzaglia, 2013; Wang et al., 2015).

264
265
266 93 Terraces as geomorphic markers to assess fluvial incision and landscape development
267
268
269 94 have been commonly used worldwide under different orogenic and post-orogenic
270
271 95 geodynamic contexts. At a regional scale, deciphering the nature and history of fluvial
272
273 96 incision in the Iberian Peninsula, which has an extensive network of terraces, has been
274
275
276 97 limited and remains an unsolved challenge. Undoubtedly, the general lack of well
277
278 98 chronologically referenced terrace systems (Santisteban and Schulte, 2007) is
279
280 99 determinant. Several regional studies on river incision have been reported by Cunha et
281
282 100 al. (2005, 2008, 2012) and Martins et al. (2009, 2010) in the Portuguese reach of the
283
284 101 Tagus River, Antón et al. (2012) and Silva et al. (2013, 2016) in the Spanish reaches of
285
286
287 102 the Duero and Tagus rivers, Stange et al. (2013; 2016) in the Segre River valley in the
288
289 103 southern Pyrenees, Soria-Jáuregui et al. (2016) in the upper sector of the Ebro River
290
291 104 valley, Scotti et al. (2014) and Giacheta et al. (2015) in the Iberian Ranges (NE Spain),
292
293
294
295

296
297
298
299
300
301
302
303
304
305
306
307
308
309
310
311
312
313
314
315
316
317
318
319
320
321
322
323
324
325
326
327
328
329
330
331
332
333
334
335
336
337
338
339
340
341
342
343
344
345
346
347
348
349
350
351
352
353
354

105 and Viveen et al. (2014) in the Miño River basin from northwest Iberian. Additionally,
106 data on regional fluvial incision need to be integrated within the geodynamic models
107 explaining the Iberian topography and with the regional Pleistocene climate
108 reconstruction for southwestern Europe.

109 The Spanish Pyrenees and the adjacent Ebro foreland basin comprise an outstanding
110 area to deduce post-orogenic river incision rates and landscape development from
111 staircase terraces and to discuss the uplift mechanisms and the climate changes
112 involved. In this paper we use a well characterized sequence of staircase terraces
113 located along the Cinca River valley, one of the most important Pyrenean tributaries of
114 the Ebro River in northeast Iberia, to evaluate post-tectonic landscape evolution.

115 Reported results are based in a combination of (i) reconstructed longitudinal strath
116 profiles starting from previously mapped terraces (Sancho, 1988), (ii) numerical ages
117 using optically stimulated luminescence (OSL) and supported by time-related trends in
118 soil development (Lewis et al., 2009), and (iii) new palaeomagnetic and soil
119 stratigraphic data. We use our results to deduce spatial and temporal patterns in river
120 incision rates and to discuss the combined action of uplifting and climate change
121 governing the formation of staircase terrace sequences in NE Iberia.

2. Study area

2.1 The Cinca River valley

124 The Cinca River valley straddles the south-central Pyrenees and the northern Ebro
125 basin (NE Spain) (Figs. 1, 2A). Mean annual precipitation varies from > 2,000 mm in the
126 high Pyrenees to < 400 mm in the semiarid Ebro basin. The Cinca River is 170 km long;

355
356
357 127 it has a drainage area of 9,700 km² and a mean annual flood discharge of 79 m³/s. The
358
359 128 natural fluvial regime of the Cinca River is altered by the presence of two large
360
361
362 129 reservoirs: the El Grado and Mediano dams (Fig. 3A).
363
364

365 130 The headwaters area of the Cinca River is glaciated and is located in the Pyrenean
366
367 131 Internal Sierras (Monte Perdido summit: 3,355 m a.s.l.). The Cinca River drains to the
368
369 132 south and is perpendicular to the Pyrenean belt, joining the larger and eastward-
370
371
372 133 flowing Ebro River in the Ribarroja reservoir (90 m a.s.l.) in the central Ebro Basin. This
373
374 134 river confluence is more than 100 km up gradient from the Mediterranean Sea (Fig. 1).
375
376 135 The Cinca River in the upper valley (from headwaters to Ainsa; Figs. 1, 3A) is a mixed
377
378 136 bedrock-alluvial channel, whereas the Cinca River in the lower valley (from Basbastro
379
380 137 to the mouth into the Ebro River; Figs. 1, 3A) is an alluvial gravel channel. Several slight
381
382 138 knickpoints can be identified along the active channel profile: however, only the
383
384 139 knickpoint located at El Grado (External Pyrenees) is noticeable (Figs. 2B, 3A).
385
386
387
388

389 140 **2.2 Geologic setting**

390
391

392 141 Geologically, the Cinca River valley is excavated in the Pyrenean belt and the adjacent
393
394 142 Ebro foreland basin (Fig. 2A). The Pyrenees constitutes a WNW-ESE striking, narrow
395
396 143 asymmetric alpine chain with a mainly southward vergence, developed from the Late
397
398 144 Cretaceous to the Early Miocene. This structural setting was formed in response to the
399
400 145 partial subduction of the Iberian lithosphere underneath Europe (e.g., Muñoz, 2002).
401
402 146 The southern central Pyrenees comprise part of the Axial Zone, formed by a basement
403
404 147 and a series of imbricated thrust sheets, involving Mesozoic to Eocene cover rocks and
405
406 148 affecting synorogenic Tertiary materials (e.g., Martínez-Peña and Casas-Sainz, 2003).
407
408
409
410
411
412
413

414
415
416
417
418
419
420
421
422
423
424
425
426
427
428
429
430
431
432
433
434
435
436
437
438
439
440
441
442
443
444
445
446
447
448
449
450
451
452
453
454
455
456
457
458
459
460
461
462
463
464
465
466
467
468
469
470
471
472

149 Specifically, the Cinca River valley is located at the western border of the South
150 Pyrenean Central Unit that is characterized by north-south oblique structures that
151 control the north-south alignment of the Cinca River (Martínez-Peña et al., 1995).
152 From a stratigraphic point of view, the Cinca River traverses the western sector of the
153 Graus-Tremp basin (the Ainsa sub-basin) (Fig. 2B), a piggy-back basin filled with
154 Palaeocene-Eocene deposits (Puigdefábregas and Souquet, 1986).

155 The Tertiary Ebro basin was formed during the Palaeogene as a consequence of
156 flexural subsidence related to growth of the surrounding mountain chains, particularly
157 the Pyrenees. Sedimentation into the closed basin continued under conditions of
158 continental internal drainage during Oligocene and Miocene times (Muñoz et al., 2002;
159 Costa et al., 2010) (Fig. 2B). This sedimentary regime persisted until the end of the late
160 Miocene (between 12.5 and 8.5 Ma) when the internal drainage of the Ebro basin
161 ended due to aggradation of the lacustrine system and extensional geodynamic
162 conditions in the western Mediterranean basin (García-Castellanos et al., 2003). The
163 Ebro basin was subsequently opened when headward erosion of coastal drainage
164 captured the internally draining system. The Ebro sedimentary basin was then incised
165 and previous depositional units were excavated and transported to the coastal
166 Mediterranean.

167 Erosional activity of the drainage in the Pyrenees and the Ebro Basin persisted
168 throughout the Quaternary. Subsequent fluvial activity developed extensive staircase
169 terrace sequences along the Ebro drainage system (e.g., Gutiérrez and Peña, 1994;
170 Peña, 1994). The earliest evidence of alluviation in the exoreic Ebro basin is at ca. 1.28

473
474
475 171 Ma in the Alcanadre River valley, a tributary of the Cinca River (Duval et al. 2015;
476
477 Sancho et al., 2016).
478 172
479
480

481 173 **2.3 Approach to the Cinca River terrace sequence**

482
483
484 174 Two basic configurations of stream terraces, strath and fill terraces, are commonly
485
486 175 differentiated, based on the morphology of the erosional surface and thickness of
487
488 alluvial sediments (Bull, 1991; Pazzaglia, 2013). A strath terrace is characterized by a
489 176 subhorizontal erosional surface carved into bedrock mantled with a thin mobile alluvial
490
491 177 cover of a bedrock channel that does not exceed the depth of scour of the stream. In
492
493 178 contrast, fill terraces are characterized by an irregular basal surface covered by a layer
494
495 179 of thick alluvium that accumulates when the channel vertically exceeds the depth of
496
497 180 scour, during periods of valley aggradation (Wegmann and Pazzaglia, 2009; Pazzaglia,
498 180
499 181 2013). The thickness of the alluvial cover is a long-discussed criterion to distinguish
500 181
501 182 between both types of terrace (Pazzaglia, 2013). Mobile alluvial cover associated with
502 182
503 183 strath terraces rarely exceeds 5 m in thickness even for large watersheds, while
504 183
505 184 greater alluvial thickness is usually related to fill terraces (Pazzaglia, 2013).
506
507 184
508
509 185
510
511

512 186 The studied terrace sequence in the Cinca River valley consists of 10 extensive paired
513
514 187 cyclic stream terraces (Sancho, 1988; Lewis et al., 2009). The mean thickness of the
515 187
516 alluvial mantle covering the straths is around 5 m, ranging from 8 m for the oldest
517 188
518 terraces to 3 m for the youngest terraces. The general morphology of strath surfaces is
519 189
520 broadly subhorizontal. Given this description, the Cinca River terrace sequence is
521 190
522 191 closer to a strath relative to a fill terrace and displays a strath-like terrace. We
523
524 191
525
526
527
528
529
530
531

532
533
534 192 recognize that in places, a near-fill terrace configuration related to slight valley
535
536 193 aggradations could be considered.
537
538
539

540 194 **3. Methods: using terrace straths to measure river incision**

541
542
543 195 Determination of the river incision rate (e.g., Burbank and Anderson, 2001) for a point
544
545 196 along a river valley is given by the ratio between the height (m) of the terrace strath
546
547 above the active channel and the timing (ka) of terrace formation. We expanded this
548 197 approach to calculate the river incision rate between a given pair of terraces; the
549
550 198 fluvial incision rate ($I_{Q_{ti}-Q_{tj}}$) (m/ka) between any two terraces Q_{ti} and Q_{tj} , is given by the
551
552 199 relation:
553
554 200
555

$$558 \quad 201 \quad I_{Q_{ti}-Q_{tj}} = H_{Q_{ti}-Q_{tj}} / T_{Q_{ti}-Q_{tj}}$$

559
560
561 202 where $H_{Q_{ti}-Q_{tj}}$ is the difference of altitude (m) of the terrace straths Q_{ti} and Q_{tj} , and
562
563 203 $T_{Q_{ti}-Q_{tj}}$ is the elapsed time (ka) between them.
564
565
566

567 204 We use the terrace straths rather than the terrace treads to measure river incision
568
569 205 rates (Wegmann and Pazzaglia, 2009) because tread surfaces can be subsequently
570
571 206 modified through both aggradation or degradation. Observations of terrace
572
573 207 stratigraphy indicate that in places the terrace surface has been aggraded through
574
575 deposition of lateral alluvial and aeolian sediments or degraded through erosion
576 208
577 removal and lowering of the original terrace surface as indicated by severely truncated
578 209
579 or missing soil profiles.
580 210
581

582 583 211 **3.1 Height of terrace straths and the active channel**

584
585
586
587
588
589
590

591
592
593 212 Collecting and assessing height measurements of bedrock strath surfaces requires
594
595 213 compiling a detailed regional geomorphological framework. Geomorphic mapping was
596
597
598 214 undertaken on an aerial photographic base (1:18,000 in scale) and was extensively
599
600 215 field checked along the Cinca River valley. Ten terraces were firstly identified (Qt1 to
601
602 216 Qt10, from higher to lower) from their altitudinal position (Sancho, 1988; Lewis et al.,
603
604 217 2009). Correlation of terraces was primarily based on geomorphologic and
605
606
607 218 stratigraphic relationships between terraces and was reinforced with soil development
608
609 219 and numerical dating. Elevations of the differentiated strath terrace surfaces and the
610
611 220 Cinca active channel were measured to sub-meter accuracy using a global positioning
612
613 221 system (GPS) differentially corrected to a permanent base station. Measurements
614
615
616 222 were occasionally supplemented by data from 1:25,000-scale topographic maps.
617
618 223 Height measurements allowed reconstruction of accurate profiles of strath terraces
619
620 224 and the active channel.

623 624 225 **3.2 Chronology of terraces**

625
626
627 226 Timing of strath preservation is broadly based on the basal age of overlying fluvial
628
629 227 deposits. We used numerical dates previously provided by Lewis et al. (2009), based on
630
631 228 OSL of quartz grains dating and supported by soil stratigraphy. These data are available
632
633
634 229 only for the lower terraces (from Qt5 to Qt9) corresponding to both the Penultimate
635
636 230 and the Last Glacial cycles. In this study we provide new chronological evidence for the
637
638 231 older terraces using paleomagnetic analysis and time-related trends in soil
639
640
641 232 development.

642 643 644 233 **3.2.1 Paleomagnetic sampling and laboratory procedures**

645
646
647
648
649

650
651
652 234 Characterization of the paleomagnetic polarity has been a powerful tool for unravelling
653
654 235 terrace ages since the pioneering work of Pevzner (1970). Subsequent applications
655
656
657 236 have focused on locating the Brunhes/Matuyama (B/M) boundary (Dubar and Semah,
658
659 237 1986; Jacobson et al., 1988) or even shorter polarity events within the Brunhes and
660
661 238 Matuyama periods (Li et al., 1997). Paleomagnetic analysis was conducted on the Cinca
662
663 239 River alluvium overlying the strath terraces to identify the location of the B/M
664
665 240 boundary. Previous results in the Central Ebro Basin (Gil et al., 2013) and in the
666
667 Alcanadre River (tributary of the Cinca River; Calle et al., 2015; Sancho et al., 2016)
668 241
669 allowed us to be confident of the suitability of the method provided that an adequate
670 242
671 sampling was guaranteed (Gil Garbi, 2017).
672 243
673
674
675 244 Sampling for paleomagnetic analysis was performed in 13 pits excavated in the upper
676
677 terraces along the valley (from Qt1 to Qt7). Siltstone layers within alluvial sequences
678 245
679 were the main targets to ensure a stable paleomagnetic signal. Sampling tools
680 246
681 designed for unconsolidated sediments were used instead standard drilling machines.
682 247
683 Subsequent consolidating techniques using non-magnetic chemical compounds
684 248
685 (sodium silicate and alumina cement) were used to obtain standard and stable
686 249
687 paleomagnetic specimens (Pueyo et al., 2006). Oriented blocks were occasionally
688 250
689 sampled.
690 251
691
692
693
694 252 Present-day declination (~ 1° 30'W) during the sampling was corrected in the core
695
696 orientations (NOAA's National Geophysical Data Center, <https://www.ngdc.noaa.gov/>).
697 253
698 Stepwise and detailed demagnetisation (both thermal [TH] and alternating field [AF])
699 254
700 was conducted in the paleomagnetic laboratory at the University of New Mexico
701 255
702 (UNM) (Albuquerque) and at the Institute of Earth Sciences "Jaume Almera" (Consejo
703 256
704
705
706
707
708

709
710
711 Superior de Investigaciones Científicas-Universitat de Barcelona). TH demagnetisation
712 257
713 was run with a TSD-1 furnace (Shonsted Ltd.), and remanent magnetization was
714 258
715 measured with a 2G three-axis SQUID magnetometer in both laboratories. The 2G-AF
716 259
717 demagnetizer was only used in the UNM laboratory.
718 260
719
720

721 Thermal stepwise demagnetisation used intervals of 50°C between room temperature
722 261
723 and 550-600°C and AF increments between 3 and 10 mT up to 100mT (following an
724 262
725 exponential trend) were run to characterize all paleomagnetic components of the
726 263
727 NRM. Paleomagnetic directions were fitted by principal components analysis (PCA;
728 264
729 Kirschvink, 1980) using the Paldir software by Utrecht Universiteit. In some cases,
730 265
731 demagnetization circles (Bailey and Halls, 1978), the stacking routine (Scheepers and
732 266
733 Zijdeveld, 1992) and the virtual directions method (Ramón and Pueyo, 2017) were
734
735 267
736 used to double-check the PCA results. Site means and terrace means were fitted by
737 268
738 Fisher (1953) statistics. It is a probability distribution for multivariate directional data
739 269
740 (vectors or simple lines in the 3D space).
741
742 270
743
744

745 271 *3.2.3 Soil development*

746
747

748 272 Soil development indices were used locally and regionally to correlate principal terrace
749
750 levels (Lewis et al., 2009) and to estimate the age of the Qt3 terrace. Soils were
751 273
752 described according to standard methods and nomenclature of the U.S. Soil Survey
753 274
754 Staff (1993). Carbonate stage morphology follows nomenclature of Gile et al. (1981)
755 275
756 and Birkeland (1999). Time-related changes in soil morphology were analyzed using a
757 276
758 well-tested soil development index (SDI) (Harden, 1982; Harden and Taylor, 1983;
759
760 277
761 McDonald et al., 1996) based on a soil chronofunction presented in Lewis et al. (2009).
762 278
763
764
765
766
767

768
769
770 279 SDI values were calculated using a conversion of soil morphologic properties
771
772 280 (rubification, texture, structure, dry consistence, moist consistence, secondary
773
774
775 281 carbonates, lightening, and argillans) into numerical data to enable a quantitative
776
777 282 comparison of the degree of soil development. Horizon Development Index (HDI)
778
779 283 values are obtained by normalizing each set of properties and a Profile Development
780
781
782 284 Index (PDI) is calculated from HDI values and horizon thickness. The PDI values reflect
783
784 285 the overall degree of soil development and provide a means of comparison among
785
786 286 soils within a given sequence or area. The PDI has proven useful for providing
787
788 287 correlations and calibrated age estimates for the sequence of strath terraces from the
789
790
791 288 Cinca River valley (Lewis et al., 2009).

792 793 794 289 **4. Results**

795 796 797 290 ***4.1 Morphopedosedimentary characteristics of the staircase terrace sequence***

798
799
800 291 The marked vertical separation between adjacent terraces, reinforced with extensive
801
802
803 292 outcrops and their longitudinal continuity, facilitated mapping, regional correlation of
804
805 293 terrace remnants, and descriptions of the fluvial terrace deposits along 170 km in the
806
807 294 Cinca River valley (Figs. 3, 4). Ten paired staircase terraces (numbered Qt1, Qt2, Qt3,
808
809
810 295 Qt4, Qt5, Qt6, Qt7, Qt8, Qt9, and Qt10, from oldest to youngest) have been preserved
811
812 296 (Appendix 1). The terrace development and preservation are prominently displayed in
813
814 297 the upper reach of the valley (near Ainsa, 50 km from the headwaters) and
815
816 298 immediately downstream of the confluence with the Ara River (Figs. 3B, 4A, D). Mean
817
818
819 299 height of the terrace straths above the active channel of the Cinca River in this sector
820
821 300 are 172.5 m (Qt3), 44.2 m (Qt7) and 6.0 m (Qt9) (Table 1). The corresponding vertical
822
823
824
825
826

827
828
829
830
831
832
833
834
835
836
837
838
839
840
841
842
843
844
845
846
847
848
849
850
851
852
853
854
855
856
857
858
859
860
861
862
863
864
865
866
867
868
869
870
871
872
873
874
875
876
877
878
879
880
881
882
883
884
885

301 separations between adjacent preserved strath terraces are 128.3 m (Qt3-Qt7) and
302 38.2 m (Qt7-Qt9) respectively.

303 The lower reach of the valley goes from the External Pyrenees, where the Cinca River
304 enters into the Ebro Basin, to the confluence with the Ebro River, including several
305 important tributary junctions (the Esera, Vero and Alcanadre rivers). The lower reach
306 shows the widest and best preserved terraces (Fig. 4B, E, F), particularly in the
307 Albalate-Belver sector (125 km from the headwaters; Fig. 3C). Mean height of the
308 terrace straths above the active channel of the Cinca River in this sector are 182.1 m
309 (Qt1), 132.5 m (Qt2), 103.5 m (Qt3), 91.3 m (Qt4), 79.9 m (Qt5), 60.4 m (Qt6), 33.9 m
310 (Qt7), 13.1 m (Qt8) and 3.6 m (Qt9) (Table 1). The corresponding vertical separations
311 between adjacent strath terraces are 49.6 m (Qt1-Qt2), 29.0 m (Qt2-Qt3), 12.2 m (Qt3-
312 Qt4), 11.4 m (Qt4-Qt5), 19.5 m (Qt5-Qt6), 26.5 m (Qt6-Qt7), 20.8 m (Qt7-Qt8) and 9.5
313 m (Qt8-Qt9).

314 Terraces Qt3, Qt7 and Qt9 are broadly preserved along the Cinca River valley
315 (Appendix 1). Terraces older than Qt7 are preserved only on the river's east bank,
316 indicating the westward migration of the Cinca River. This migration is well noted in
317 the Albalate-Belver sector and reaches a lateral westward displacement of 8 km
318 between Qt1 at Monte Julia and Qt7 at Albalate (Fig. 3C). Qt7 and subsequent Qt8 and
319 Qt9 terraces outcrop in both sides of the valley. This implies a significant change in the
320 width of the valley. In fact, Qt7 is approximately 5 km wide in the Albalate-Alcolea
321 section, whereas the current valley bottom (active channel and floodplain) reaches a
322 maximum width of 2 km (Fig. 3C).

886
887
888
889
890
891
892
893
894
895
896
897
898
899
900
901
902
903
904
905
906
907
908
909
910
911
912
913
914
915
916
917
918
919
920
921
922
923
924
925
926
927
928
929
930
931
932
933
934
935
936
937
938
939
940
941
942
943
944

323 Terrace treads are typically broad (2-4 km width) and commonly underlain by 2.8-7.7
324 m (Fig. 4C) of largely cobble-rich gravel with a sand-rich matrix, large (20-100 cm
325 diameter) sub-rounded boulders, sparsely populated with sand lenses, and capped by
326 either gravelly sand-rich alluvium or finer-textured overbank deposits. Fluvial deposits
327 occur in fining-upwards sequences. According to lithofacies of Miall (1978), gravels are
328 generally massive but locally imbricated (Gm) and cross-stratified (Gt, Gp), are well-
329 sorted and sub-rounded and consist of limestone, sandstone, granite, quartzite, and
330 schist (in order of decreasing abundance) of Pyrenean and, locally, Ebro basin
331 provenances. Interbedded sand lenses can be cross-stratified (St, Sp) or horizontally
332 laminated (Sh). Gravels can be capped by overbank silts (Fm).

333 Strath surfaces are carved into Cretaceous to Eocene marine carbonates and marls
334 (Fig. 4A) along the river's Pyrenean reach and Eocene-Miocene continental deposits
335 (Fig. 4B) along the Ebro Basin reach (Fig. 2B; Appendices 1 and 2). Localized
336 deformation of the strath surface and associated gravels (e.g., tilting and faulting)
337 occurs in places and is related to salt diapirism and gypsum dissolution confined to the
338 Barbastro anticline and the Estada-Estadilla diapir (Sancho, 1988, 1989; Lucha et al.,
339 2008) (Appendix 1). Local deformation related to small vertical faults was also
340 observed near El Grado and El Pueyo de Araguás.

341 The Qt1 terrace is poorly preserved and only occurs between Albalate and Binaced
342 (Figs. 3C, 4F; Appendix 1), where remnants occur as isolated hills (San Salvador and Las
343 Brujas sites). The Qt1 remnants constitute the highest preserved remnants of the Cinca
344 River terrace sequence. Mean thickness of alluvial cover is around 7.7 m and maximum
345 grain size (Dmax) ranges from 30-48 cm (mean value 42 ± 9 cm) (Appendix 2). An

945
946
947
948 346 eroded petrocalcic soil horizon (~1 m thick) formed in fine-grained sediments is
949
950 347 preserved in places.

951
952
953 348 The Qt2 strath terrace is more or less continuously preserved between Albalate and
954
955 349 Belver and is in the vicinity of the Qt1 remnants (Figs. 3C; Appendix 1). Mean thickness
956
957
958 350 of alluvial cover preserved is around 5.6 m and maximum grain size (D_{max}) ranges
959
960 351 from 36-48 cm (mean value 41 ± 4 cm) (Appendix 2). The soils found on the Qt2 are only
961
962 352 weakly to moderately developed and are considerably less developed than the soils on
963
964
965 353 the younger Qt3 terrace. This indicates that the original terrace surface has been
966
967 354 severely eroded.

968
969
970 355 The Qt3 terrace is one of the two most important geomorphic features along the Cinca
971
972 356 River valley. It is preserved continuously in the lower reach of the valley between
973
974
975 357 Monzón and Fraga (Figs. 3C, 4F; Appendix 1); other relevant outcrops have been
976
977 358 identified at Barbastro, El Grado and Ainsa (Figs. 3B, 4D; Appendix 1). Mean thickness
978
979 359 of alluvial cover is around 5.8 m and maximum grain size (D_{max}) ranges from 26-50 cm
980
981 360 (mean value 34 ± 6 cm) (Fig. 5; Appendix 2). Locally the Qt3 deposit near El Grado is
982
983 361 faulted. Soil characteristics on this terrace are described below.

984
985
986
987 362 The Qt4 terrace is preserved only between Barbastro and Fraga (Figs. 3C, 4E; Appendix
988
989 363 1). Mean thickness of alluvial cover is around 5.2 m and maximum grain size (D_{max})
990
991
992 364 ranges from 26-43 cm (mean value 35 ± 8 cm) (Appendix 2). Near Belver, the terrace
993
994 365 deposits include a 90 cm-thick aeolian cap that overlies 90 cm of overbank fines. An
995
996 366 OSL date on the loess cap constrains its age to be 20 ± 3 ka (Lewis et al., 2009), likely
997
998 367 deposited during the MIS2 glaciation. No soils were described on the Qt4 terrace due
999
1000
1001
1002
1003

1004
1005
1006 368 to surface erosion. In some localities, reworking of the Qt4 surface is evidenced by a
1007
1008
1009 369 cap of colluvium incorporating pieces of underlying petrocalcic horizons.
1010
1011

1012 370 The Qt5 terrace is also preserved only between Monzón and Fraga Fraga (Fig. 3C;
1013
1014 371 Appendix 1). Stratigraphic relations between the Qt4 and Qt5 terraces indicate that
1015
1016 372 formation of the Qt5 terrace cannibalized much of the older Qt4 terrace. Mean
1017
1018
1019 373 thickness of alluvial cover is around 4.5 m and maximum grain size (D_{max}) ranges from
1020
1021 374 28-51 cm (mean value 38 ± 7 cm) (Appendix 2). North of Castejón del Puente, the Qt5
1022
1023 375 terrace was deformed by the diapiric activity of the Barbastro salt anticline (Sancho,
1024
1025
1026 376 1989). The Qt5 soils in the Albalate sector have well developed Bk and Bkm horizons
1027
1028 377 with stage III+ to IV+ carbonate morphology (Table 2) (Lewis et al., 2009).
1029
1030

1031 378 The Qt6 terrace is also preserved only between Monzón and Fraga Fraga (Figs. 3C;
1032
1033 379 Appendix 1) and exposures of the deposits are very limited because the degradation of
1034
1035
1036 380 the scarps. Mean thickness of alluvial cover is around 5.1 m and maximum grain size
1037
1038 381 (D_{max}) ranges from 24-80 cm (mean value 39 ± 19 cm) (Appendix 2). Soils have a well-
1039
1040 382 developed Btk horizon and stage III+ carbonate morphology (Table 2) (Lewis et al.,
1041
1042 383 2009).
1043
1044
1045

1046 384 Remnants of the Qt7 terrace occur continuously along approximately 120 km of the
1047
1048 385 Cinca valley (Figs. 3B, C, 4; Appendix 1). This is the best-preserved terrace on the Cinca
1049
1050 386 and the most relevant terrace marker in the landscape. Terrace remnants are broad
1051
1052 387 and up to 4 km in width along the lower reach. Mean thickness of alluvial cover is
1053
1054
1055 388 around 5 m. Maximum grain size (D_{max}) ranges from 20-68 cm (mean value 34 ± 9 cm)
1056
1057 389 (Fig. 5; Appendix 2). Local distribution of terraces in the Albalate area suggests that
1058
1059
1060
1061
1062

1063
1064
1065
1066 390
1067
1068 391
1069
1070 392
1071
1072 393
1073
1074 394
1075
1076
1077 395
1078
1079 396
1080
1081 397
1082
1083
1084
1085 398
1086
1087 399
1088
1089 400
1090
1091 401
1092
1093
1094 402
1095
1096 403
1097
1098
1099 404
1100
1101 405
1102
1103
1104 406
1105
1106 407
1107
1108 408
1109
1110 409
1111
1112
1113 410
1114
1115 411
1116
1117
1118
1119
1120
1121

Qt7 terrace formation cannibalized much of older Qt6 and Qt5 terraces. In some locations, there is 3-4 m of colluvium on top of the Qt7 fluvial deposits. The Qt7 strath surface and overlying deposits are deformed when the underlying bedrock is composed of Upper Triassic evaporites and clays (Estada-Estadilla diapir) and Eocene evaporites (Barbastro salt anticline) (Sancho, 1989; Lucha et al., 2008). Local small faults deform the Qt7 deposits at El Pueyo de Araguás. The Qt7 soils in the Albalate sector have moderately to well-developed Btk horizons and stage II to weak stage III carbonate morphology (Table 2) (Lewis et al., 2009).

The Qt8 terrace is not as extensively preserved as Qt7; it crops out only along the lower 35 km of the valley (Fig. 3C; Appendix 1), where it is 2-3 km wide. Mean thickness of alluvial cover is around 2.7 m and maximum grain size (D_{max}) ranges from 22-42 cm (mean value 29 ± 6 cm) (Appendix 2). Soils in the Albalate sector have moderately developed Btk horizons with stage II carbonate morphology (Table 2) (Lewis et al., 2009).

The Qt9 terrace is generally co-extensive with the Qt7 terrace and traceable along 140 km of the total length of the river valley (Figs. 3B, C, 4D, E, F; Appendix 1). The Qt9 terrace is also largely co-extensive with Qt8, where the latter is preserved, and is approximately 2 km wide. Maximum grain size (D_{max}) ranges from 12-60 cm (mean value 29 ± 12 cm) (Fig. 5; Appendix 2) and mean thickness of alluvial cover is around 3.3 m. Locally this terrace is considerably thicker (e.g., 10 m at Castejón del Puente) because of deposition across the synsedimentary karstic subsidence on the south flank of the Barbastro salt anticline. The Qt9 soils in the Albalate sector have moderately

1122
1123
1124
1125⁴¹² developed Bw and Bk horizons with stage I+ carbonate morphology (Table 2) (Lewis et
1126
1127⁴¹³ al., 2009).

1128
1129
1130⁴¹⁴ The Qt10 terrace (Figs. 3B, C, 4E, F), which is in an extensive active floodplain, has
1131
1132⁴¹⁵ Roman bridge abutments preserved on its top near Castejón del Puente,
1133
1134
1135⁴¹⁶ demonstrating that this has been the active surface since at least Roman times in the
1136
1137⁴¹⁷ region (from ca. 140 BC until ca. 400 AD, approximately about 2,000 years ago)
1138
1139⁴¹⁸ (Beltrán, 1985).

1140 1141 1142⁴¹⁹ **4.2 Terrace profiles** 1143 1144

1145
1146⁴²⁰ The longitudinal profiles of the terrace straths and the active channel of the Cinca
1147
1148⁴²¹ River were reconstructed (Fig. 6) from 300 GPS measurements (Appendices 1 and 2)
1149
1150⁴²² and a few elevations derived from topographic maps. Strath heights (projected to a
1151
1152⁴²³ common vertical plane down the center of the modern stream valley) reveal several
1153
1154
1155⁴²⁴ consistent patterns along the length of the Cinca River from headwaters to its
1156
1157⁴²⁵ confluence with the Ebro River. Several key features of the terrace profiles are
1158
1159⁴²⁶ significant.

1160
1161
1162
1163⁴²⁷ First, the Cinca River has experienced progressive fluvial incision subsequent to
1164
1165⁴²⁸ formation of the Qt1 terrace, producing a marked vertical separation among terraces
1166
1167⁴²⁹ (Fig. 6; Table 1). As a consequence, a noticeable and well expressed staircase pattern
1168
1169⁴³⁰ has developed along the valley.

1170
1171
1172
1173⁴³¹ Second, overall longitudinal profiles are semi-parallel with a slight, but clear, upstream
1174
1175⁴³² divergence (Fig. 6). The greatest expression of divergence is recorded by the Qt3
1176
1177⁴³³ terrace with vertical separation between the active channel and strath surface ranging
1178
1179
1180

1181
1182
1183
1184⁴³⁴ from 165-175 m near Ainsa (km 50), 130-135 m at Barbastro (km 100) and 95-105 m at
1185
1186⁴³⁵ Zaidín (km 155). Locally variable effects in divergence are observed along the profile
1187
1188⁴³⁶ due to rock resistance, active faulting, and gypsum diapirism and dissolution; however,
1189
1190⁴³⁷ these effects cannot explain the first-order longitudinal trends. The Qt7 profile also
1191
1192⁴³⁸ diverges upstream with respect to the active channel, although not as markedly. For
1193
1194
1195⁴³⁹ example, the Qt7 is 45-50 m above the active channel near Ainsa, 40 m at Barbastro
1196
1197⁴⁴⁰ and 30-35 m near Zaidín.

1198
1199
1200⁴⁴¹ The log plot of longitudinal profiles also shows changes in gradient at the Pyrenean
1201
1202
1203⁴⁴² mountain front. A prominent knickpoint occurs in the active channel at 90 km from the
1204
1205⁴⁴³ headwaters near El Grado (Fig. 6). This knickpoint is related to the higher erosional
1206
1207⁴⁴⁴ resistance of the folded rocks (Cretaceous and Eocene limestones) of the External
1208
1209⁴⁴⁵ Pyrenees (Fig. 2B; Appendix 1), as opposed to less resistant clastic sedimentary rocks
1210
1211⁴⁴⁶ at the margin of the Ebro basin. The knickpoint appears to be spatially fixed because its
1212
1213
1214⁴⁴⁷ location has persisted through time for straths associated with Qt3, Qt7, Qt9 terraces
1215
1216⁴⁴⁸ and the active channel.

1217 1218 1219⁴⁴⁹ **4.3 Terrace chronology**

1220 1221 1222 1223⁴⁵⁰ **4.3.1 Geochronology for terraces Qt5 to Qt9**

1224
1225
1226⁴⁵¹ Numerical ages of the five youngest terraces (Qt5, Qt6, Qt7, Qt8, and Qt9) (Table 3) of
1227
1228⁴⁵² the Cinca River sequence have been previously reported by Lewis et al. (2009), from
1229
1230
1231⁴⁵³ multiple OSL dates and reinforced using regional soil stratigraphy. To summarize, Lewis
1232
1233⁴⁵⁴ et al. (2009) obtained two dates for Qt5 terrace (171 ± 22 ka and 180 ± 12 ka), giving a
1234
1235⁴⁵⁵ weighted mean age of 178 ± 21 ka, and one date for Qt6 (97 ± 16 ka). Six samples from
1236
1237
1238
1239

1240
1241
1242
1243⁴⁵⁶ Qt7 terrace constitute a tightly grouped set of dates (63 ± 12 , 59 ± 13 , 64 ± 13 , 61 ± 3 ,
1244
1245⁴⁵⁷ 56 ± 4 and 65 ± 5) with a weighted mean age of 61 ± 4 ka. Five dates on Qt8 terrace (39
1246
1247⁴⁵⁸ ± 5 , 42 ± 6 , 47 ± 4 , 50 ± 4 and 50 ± 3) gave a weighted mean age of 47 ± 4 ka. Finally,
1248
1249⁴⁵⁹ eight well grouped OSL dates for Qt9 terrace gave a weighted mean age of 11 ± 1 ka.
1250
1251⁴⁶⁰ The Qt7 terrace is correlated with glacial and fluvioglacial deposits in the Cinca
1252
1253
1254⁴⁶¹ headwaters (confluence of the Cinca and Cinqueta rivers at Mesón de Salinas) (Fig. 3A)
1255
1256⁴⁶² that have a mean age of 64 ± 11 ka, corresponding to the last maximum glacier
1257
1258⁴⁶³ extension in the south-central Pyrenees (Sancho et al., 2003). More detailed
1259
1260⁴⁶⁴ information from OSL measurements and derivation of mean terrace deposit dates is
1261
1262
1263⁴⁶⁵ presented in Lewis et al. (2009).

1264 1265 1266⁴⁶⁶ 4.3.2 Paleomagnetic data

1267
1268
1269⁴⁶⁷ The intensity of the NRM from terrace deposits of the Cinca River ranged in intensity
1270
1271
1272⁴⁶⁸ from 0.132 to 317 mA/m with an average of 39.98 mA/m (± 3.8 mA/m), although 90%
1273
1274⁴⁶⁹ of the data were between 0.4 and 200 mA/m (Fig. 7A). After spurious components at
1275
1276⁴⁷⁰ very low temperatures (below 200°C), with occasional large intensities, stable
1277
1278⁴⁷¹ paleomagnetic directions were observed between 250 °C and 560-600 °C in the
1279
1280
1281⁴⁷² thermal treatment (Fig. 7B). Alternating field treatment was not as successful in
1282
1283⁴⁷³ isolating stable directions, although some reliable directions (comparable to TH sister
1284
1285⁴⁷⁴ samples) were identified from 8-10 mT up to 40 mT (and even 80 mT; see for example
1286
1287⁴⁷⁵ samples 77a and 77b) (Fig. 7B). The primary and stable component of the magnetic
1288
1289
1290⁴⁷⁶ field is characterized by low-coercivity and medium-temperature minerals pointing to
1291
1292⁴⁷⁷ magnetite as the main carrier of the magnetization.
1293
1294
1295
1296
1297
1298

1299
1300
1301 478 Lower and intermediate terraces (from Qt9 to Qt3) unambiguously registered normal
1302 polarity of the primary paleomagnetic field (Fig. 7C). On the other hand, the high level
1303
1304 479 Qt2 terrace unequivocally recorded a reversed polarity. This crucial observation is well
1305 supported by the consistent directions obtained in three different pits (T9-1, T9-2 and
1306 480 T9-3) in the Mombrún area (near Albalate) (Table 4). The oldest terrace (Qt1) recorded
1307 an intermediate pattern, displaying both polarities and scattered directions, although
1308 481 only one pit was sampled in this terrace. Paleomagnetic directions found in the Cinca
1309 terrace sequence, therefore, are consistent (equal demagnetization intervals and
1310 482 carriers), display pseudo-antipodal polarities (N: 355, 58 [α_{95} : 10.6° and k: 5.7]; R:
1311 220, -48 [α_{95} : 20.6° and k: 5.74]) and seem to be a reliable record of the primary
1312 paleomagnetic field (Fig. 7C).
1313 483
1314
1315 484
1316
1317 485
1318
1319 486
1320
1321
1322 487
1323
1324 488
1325
1326

1327 489 Despite individual paleomagnetic means that were weakly defined partially due to the
1328 small number of demagnetized samples (Table 4), the mean directions and polarities
1329 490 were consistent among the different samples sites across the same terrace. Besides,
1330 the stereographic projection merging all data together gives robust and pseudo-
1331 antipodal means that allow us to be confident about the primary character of the
1332 491 magnetic record.
1333
1334 492
1335
1336 493
1337
1338 494
1339
1340
1341

1342 495 In view of these results, a relative chronology can be established (Table 1). All studied
1343 terraces younger than Qt3 display a normal polarity and belong to the Brunhes period
1344 496 in agreement with the available OSL dates for Qt5 to Qt9. The Qt2 terrace must belong
1345 to the Matuyama reverse period, likely close to the Brunhes/Matuyama reversal, and
1346 497 its boundary (C1r/C1n: 0.773 Ma) (Singer, 2014) must be located between the Qt3 and
1347 Qt2 terraces. The poor results found in the Qt1 terrace prevent the proposal of any
1348
1349 498
1350
1351 499
1352
1353 500
1354
1355
1356
1357

1358
1359
1360
1361 501 reliable interpretation, although they point to the occurrence of another zone with
1362
1363 502 normal polarity. Future chronologic studies may shed light on interpretation and
1364
1365 503 distinguish between Jaramillo and Cobb Mt. normal events. These two hypotheses
1366
1367 504 have been recently proposed in other locations in the Ebro Basin (Sancho et al. 2016;
1368
1369 505 Gil et al., in review).

1371 1372 1373 506 *4.3.4 Qt3 soil characteristics and estimated soil age*

1374
1375
1376 507 Soils formed on the Qt3 surfaces along the upper (Ainsa) and lower (Albalate) reaches
1377
1378 508 of the Cinca River valley have the strongest degree of development relative to soils
1379
1380
1381 509 formed on the younger terraces (Table 2). Soils on the Qt3 terrace near Albalate vary
1382
1383 510 in development, reflecting soils that have formed in either the original cobble-gravel
1384
1385 511 bar deposits or in the original channel settings where the soil parent material consist of
1386
1387 512 fine-textured overbank (with possible aeolian contributions) that overlies gravel-rich
1388
1389 513 alluvium. Soils formed in depositional bars have weakly developed Btk horizons that
1390
1391
1392 514 overlie well-developed Bkm horizons with Stage IV to V carbonate morphology. Soils
1393
1394 515 formed in channel settings have weak- to moderately-developed Btk horizons with
1395
1396 516 stage IV carbonate morphology. Soil depth to the Bkm horizons ranges from 35 to 88
1397
1398
1399 517 cm and occurs at a shallower depth for soils formed in bar deposits. Soil PDI (profile
1400
1401 518 development index) values range from 61.4 to 80.8 for the Qt3 soils (Table 2).

1402
1403
1404 519 By comparison, soils formed on the Qt3 terrace surface near Ainsa reflect soil
1405
1406
1407 520 formation under a much wetter subhumid climate. Soil development primarily consists
1408
1409 521 of very thick soil Bt horizons with patchy to nearly continuous coatings of clay along
1410
1411 522 pores, ped faces and gravels. B horizon thickness on the Qt3 surface exceeds 300 cm.
1412
1413
1414
1415
1416

1417
1418
1419
1420⁵²³ There is no carbonate accumulation in Qt3 terrace soils along the upper reach of the
1421
1422⁵²⁴ Rio Cinca valley due to the high effective soil moisture. The only soil described on the
1423
1424⁵²⁵ Qt3 surface near Ainsa has a PDI value of 105.1 (Table 2). The higher value reflects the
1425
1426⁵²⁶ greater degree of soil development that has occurred under the more humid climate at
1427
1428
1429⁵²⁷ Ainsa sector relative to soils forming near the Albalate sector.

1430
1431
1432⁵²⁸ Soil age estimates for the Qt3 were based on the soil chronofunction developed by
1433
1434⁵²⁹ Lewis et al. (2009) and the PDI values calculated for the five soils described near
1435
1436⁵³⁰ Albalate. We did not include the Ainsa Qt3 soil because its more humid soil
1437
1438
1439⁵³¹ environment is not compatible with the soil chronofunction developed for soils in
1440
1441⁵³² more arid settings. Soil age estimates (based on each PDI value; Table 2) ranged from
1442
1443⁵³³ 291 to 565 ka; mean age was 401 ± 117 ka (Table 1). The Qt3 soils were better
1444
1445⁵³⁴ developed than soils formed on the Qt5 surface, which is approximately 178 ka (Table
1446
1447
1448⁵³⁵ 2).

1450 1451⁵³⁶ **4.4 Incision rates**

1452
1453
1454⁵³⁷ River incision rates have been calculated by comparing the vertical separation (m) and
1455
1456
1457⁵³⁸ the elapsed time (ka) between successive terrace strath surfaces. For this level of
1458
1459⁵³⁹ analysis, we considered that strath formation and the deposition of the corresponding
1460
1461⁵⁴⁰ alluvium are generally synchronous in time. The terrace sequences at Ainsa (kilometer
1462
1463⁵⁴¹ 50 from headwaters; upper valley reach) and at Albalate (kilometer 125 from
1464
1465
1466⁵⁴² headwaters; lower valley reach) sectors (Fig. 6) were selected because of the extensive
1467
1468⁵⁴³ presence of well-preserved terrace remnants in both areas (Figs. 3B, C, 4D, F).

1469
1470⁵⁴⁴ Differential mean heights, elapsed mean time and mean incision rates for the selected
1471
1472
1473
1474
1475

1476
1477
1478
1479⁵⁴⁵
1480
1481⁵⁴⁶
1482
1483⁵⁴⁷
1484
1485
1486⁵⁴⁸
1487
1488
1489⁵⁴⁹
1490
1491⁵⁵⁰
1492
1493⁵⁵¹
1494
1495⁵⁵²
1496
1497
1498⁵⁵³
1499
1500⁵⁵⁴
1501
1502⁵⁵⁵
1503
1504
1505⁵⁵⁶
1506
1507⁵⁵⁷
1508
1509⁵⁵⁸
1510
1511⁵⁵⁹
1512
1513
1514
1515⁵⁶⁰
1516
1517⁵⁶¹
1518
1519⁵⁶²
1520
1521⁵⁶³
1522
1523
1524⁵⁶⁴
1525
1526⁵⁶⁵
1527
1528⁵⁶⁶
1529
1530⁵⁶⁷
1531
1532
1533
1534

sets of coupled terraces are summarized in Table 5. Uncertainties in numerical dating were also considered to present maximum and minimum fluvial incision rates (Table 5).

Considering mean incisions from the coupled successions Qt3-Qt7, Qt7-Qt9 and Qt9-active channel, we proposed that a regional mean fluvial incision rate of 0.47 m ka^{-1} occurred during the Middle and Late Pleistocene. The spatial and temporal patterns of river incision also show some singularities. Rates of fluvial incision decreased downstream from Ainsa to Albalate; mean incision rates were 0.56 m ka^{-1} at Ainsa and 0.38 m ka^{-1} at Albalate. Additionally, the mean incision rate obtained from the coupled succession Qt3-Qt7 was 0.38 m ka^{-1} at Ainsa and 0.20 m ka^{-1} at Albalate (Table 5). For the coupled succession Qt7-Qt9, values were 0.76 m ka^{-1} and 0.61 m ka^{-1} , respectively. The coupled Qt9-active channel succession indicates incision of 0.54 m ka^{-1} at Ainsa and 0.33 m ka^{-1} at Albalate. These results clearly indicate that incision rates were higher on the upper reach relative to the lower reach over the considered time intervals.

The temporal pattern of variation in incision rates along the Cinca River valley reflects important changes during the Middle and Late Pleistocene. These changes are well observed in the Albalate sector, where the more complete sequence of terraces is preserved (Table 5). The Middle Pleistocene coupled Qt3-Qt5 terraces reflects an incision rate of 0.11 m ka^{-1} . By comparison, the incision rate of 0.24 m ka^{-1} was considerably higher during the Middle-Late Pleistocene transition for the coupled Qt5-Qt6 terraces. The Cinca River attained the highest incision rates during the Late Pleistocene. Pairing the Qt6-Qt7 terraces gives an incision rate of 0.74 m ka^{-1} and the

1535
1536
1537
1538 568 coupled Qt7-Qt8 terraces yields the maximum calculated rate of 1.48 m ka⁻¹. For the
1539
1540 569 coupled Qt8-Qt9 terraces and the Qt9-Active channel, incision rates were substantially
1541
1542 570 lower: 0.26 m ka⁻¹ and 0.33 m ka⁻¹, respectively (Table 5; Fig. 8). Time-related trends in
1543
1544 571 incision rates along the Ainsa sector, where the number of couples of terraces is less,
1545
1546 572 were similar (Table 5; Fig. 8). As a consequence, the temporal incision pattern shows
1547
1548
1549 573 very low rates over the Middle Pleistocene, a gradual increase until the beginning of
1550
1551 574 the Late Pleistocene (maximum rates at 60-50 ka) and then a gradual decrease to the
1552
1553 575 present.

1554
1555
1556 576 Additionally, taking into account the proposed paleomagnetic dates for Qt1 (Jaramillo
1557
1558
1559 577 event, 999-1070 ka) and Qt2 (reversed period previous Jaramillo event, 780-999 ka) in
1560
1561 578 the Albalate sector (Table 1), we can tentatively estimate mean incision rates of 0.06 m
1562
1563 579 ka⁻¹ and 0.34 m ka⁻¹ for the coupled terraces of Qt2-Qt3 and Qt1-Qt2, respectively
1564
1565 580 (Table 5; Fig. 8).

1566 1567 1568 1569 581 **5. Discussion**

1570
1571
1572 582 Landscape evolution and regional fluvial incision reflects an integration between uplift
1573
1574 583 and climate (e.g., Whipple and Tucker, 1999; Gibbard and Lewin, 2009; Wegmann and
1575
1576 584 Pazzaglia, 2009; Westaway et al., 2009; Stokes et al., 2012; Pazzaglia, 2013). Some
1577
1578
1579 585 studies have defined the geodynamic state (e.g., Lewis et al., 2000; Cloetingh et al.,
1580
1581 586 2002; Garcia-Castellanos et al., 2003; Gunnell et al., 2008; Casas-Sainz and de Vicente,
1582
1583 587 2009; Fernández-Lozano et al., 2011) and the climate evolution based on fluvial
1584
1585
1586 588 records (Fuller et al., 1998; Lewis et al., 2009; Benito et al. 2010; García-Ruiz et al.,
1587
1588 589 2013; Whitfield et al., 2013; Sancho et al., 2015) during the Quaternary in NE Spain.
1589
1590
1591
1592
1593

The results presented above provide an opportunity to better understand the factors constraining regional and temporal fluvial incision patterns in the NE Iberian Peninsula.

5.1 Regional fluvial incision pattern

The regional pattern of the Cinca River incision can be basically defined by (i) the well-marked vertical separation between successive terrace straths, (ii) the near-parallel terrace strath profiles, and (iii) the westward migration of the Cinca River through time. The calculated mean river incision rate in the Cinca River valley (Pyrenees and Ebro Basin) during the Middle and Late Pleistocene was 0.47 m ka^{-1} . This rate is similar to channel incision rates of $\leq 1 \text{ m ka}^{-1}$ for mountainous regions where commonly paired and extensive terraces occur (Wegmann and Pazzaglia, 2009). A maximum incision rate of 0.98 m ka^{-1} in the Miranda basin (Upper Ebro river valley), also within the Pyrenees, has been indicated by Soria-Jáuregui et al. (2016). Although regional data on river incision rates across the Iberian Peninsula are limited, the topographic pattern of river incision in the Pyrenees and the Ebro Basin is clearly different than those observed in the nearby Iberian Range (Giachetta et al., 2015) or in other extensive Iberian Tertiary basins drained by rivers flowing into the Atlantic Ocean. Mean fluvial incision rates of 0.065 m ka^{-1} from the terrace sequence of the Arlanzón River (Duero Basin) have been reported by Moreno et al. (2012), and a figure of 0.05 m ka^{-1} for terraces in different river valleys in the Central Tagus Basin has been roughly estimated by Silva et al. (2013, 2016). Fluvial incision rates of $0.07\text{-}1 \text{ m ka}^{-1}$ (Cunha et al., 2005, 2008) and $0.13\text{-}0.53 \text{ m ka}^{-1}$ (Martins et al., 2009) have been calculated from terrace sequences in the Lower Tagus River basin.

1653
1654
1655 612 *5.1.1 Vertical separation between strath terraces*
1656
1657
1658

1659 613 In the Cinca River valley, vertical separation between couples of adjacent terrace
1660
1661 614 straths ranged from approximately 10 to 50 m near Albalate (Table 5). Uplift must be
1662
1663 615 sufficiently high to produce well marked altitudinal separation between terraces
1664
1665 616 (Wang et al., 2015). He et al. (2015) obtained incision rates of 0.62-1.83 m ka⁻¹ for
1666
1667
1668 617 terraces developed in rapidly uplifting mountainous areas (SE Tibetan Plateau), clearly
1669
1670 618 higher than in the Cinca River valley under post-tectonic conditions. Many studies have
1671
1672 619 demonstrated how long-term incision rates serve as a proxy for bedrock uplift rates
1673
1674 620 (Merritts et al., 1994; Bridgland, 2000; Pazzaglia and Brandon, 2001; Wegmann and
1675
1676
1677 621 Pazzaglia, 2002; Bridgland and Westaway, 2008).

1678
1679
1680 622 There are three regional geodynamic mechanisms that likely explain the geomorphic
1681
1682 623 expression of the incision of the Cinca River. First, post-orogenic lithosphere uplift in
1683
1684 624 the northeastern Iberian margin could be at least partially attributed to isostatic
1685
1686
1687 625 adjustment resulting from crustal thickening influenced by pre-existing faults (Casas-
1688
1689 626 Sainz and de Vicente, 2009; Fernández-Lozano et al., 2011).

1690
1691
1692 627 Second, lithosphere uplift could also be related to erosional unloading in the Pyrenees
1693
1694 628 and the Ebro Basin after the connection of the drainage system with the
1695
1696
1697 629 Mediterranean Sea at the end of the Late Miocene (Coney et al., 1996; Vergés et al.,
1698
1699 630 1998; Waltham et al., 2000; Garcia-Castellanos et al., 2003; Gibson et al., 2007; Stange
1700
1701 631 et al., 2016; Garcia-Castellanos and Larrasoña, 2015). Erosional denudation has
1702
1703
1704 632 prevailed for at least the last 10 Ma in the Central Pyrenees (Coney et al., 1996;
1705
1706 633 Fitzgerald et al., 1999; Garcia-Castellanos et al., 2003; Gibson et al., 2007) and
1707
1708
1709
1710
1711

1712
1713
1714
1715 634 thermochronologic (U-Th/He) data indicate uniformly low rates (0.2 mm/yr) (Gibson et
1716 al., 2007). On the other hand, it should be noted that the thickness of sedimentary fill
1717 635
1718 in the north-central sector of the Ebro basin during the Late Oligocene and Early
1719 636
1720 Miocene exceeded 5,000 m and consequently caused important flexural load effects
1721 637
1722 on the lithosphere (Gaspar-Escribano et al., 2001). Considering the topography of the
1723 638
1724 youngest Tertiary rocks (Pérez-Rivarés et al., 2002) preserved in the Central Ebro Basin
1725
1726 639
1727 (Monte Oscuro and San Caprasio, 812 m a.s.l.) and the altitude of the active Cinca
1728 640
1729 channel close to the confluence into the Ebro River (Mequinenza Reservoir, 80 m
1730 641
1731 a.s.l.), a denudation of 750 m must be considered as a minimum to explain the
1732 642
1733 erosional rebound. The flexural isostatic compensation of the eroded materials from
1734
1735 643
1736 the Ebro basin is considered by Garcia-Castellanos and Larrasoña (2015) to be the
1737 644
1738 major force driving fluvial incision and topographic development.
1739 645
1740
1741
1742
1743 646 A third factor that could also modulate Quaternary regional uplift required to develop
1744
1745 647
1746 the terrace sequence of the Cinca River is the occurrence of a warm, buoyant
1747 648
1748 asthenosphere perhaps related to adjacent active crustal extension and volcanism in
1749 649
1750 northeastern Spain (Lewis et al., 2000). This is further supported by Janssen et al.
1751
1752 650
1753 (1993) who presented a model of subsidence in the Valencia Trough and associated
1754 651
1755 uplift in the eastern Iberian margin during the Pliocene. Mantle dynamics during post-
1756 652
1757 orogenic stages may also account for the uplift in the Pyrenees and the Ebro southern
1758 653
1759 foreland basin (Stange et al., 2016). However, Garcia-Castellanos and Larrasoña
1760
1761 654
1762 (2015) considered forces related to mantle flow to have a minor role in building the
1763 655
1764 post-tectonic topography of the Ebro basin.
1765
1766
1767
1768
1769
1770

1771
1772
1773
1774 656
1775
1776 657
1777
1778 658
1779
1780 659
1781
1782 660
1783
1784
1785
1786 661

Finally, although numerical dates to establish correlations are very limited, the broadly uniform altimetry of the staircase terrace sequences in the valleys of the main tributaries flowing into the Ebro River from the Pyrenees (Noguera Ribagorzana, Cinca, Alcanadre and Gállego rivers, from east to west) is noticeable (Gutiérrez and Peña, 1994).

5.1.2 Near-parallel strath profiles

1787
1788
1789 662
1790
1791 663
1792
1793
1794 664
1795
1796 665
1797
1798 666
1799
1800 667
1801
1802
1803

In addition to vertical separation between terrace straths of the Cinca River, near-parallel concave-upward terrace profiles were also clearly demonstrated (Fig. 6). Steady regional crustal uplift would drive uniform fluvial incision and invariant incision rates, resulting in parallel terrace longitudinal profiles (Schlunegger and Hinderer, 2001; Pazzaglia, 2013). As a consequence, we postulate a trend to a uniform uplift rate over the Pleistocene in NE Iberia.

1804 668
1805
1806 669
1807
1808 670
1809
1810 671
1811
1812
1813 672
1814
1815 673
1816
1817 674
1818
1819 675
1820
1821
1822 676
1823
1824 677
1825
1826
1827
1828
1829

A weak trend upstream divergence of strath profiles was also observed. The upstream divergence among Qt3, Qt7 and Qt9 profiles includes a decrease in terrace gradient from Qt3 to Qt9 terraces (Fig. 6). The stream gradient controls both the stream-power and the transport capacity (Hack, 1973) through flow velocity. On the other hand, bedload movement by rolling is related to flow velocity near the streambed (Chorley et al., 1984). As a consequence, gravel-size transport is directly related to channel gradient. Considering the more representative strath terraces along the Cinca River valley (Qt3, Qt7 and Qt9), the maximum grain size (D_{max}) (34 ± 6 cm, 34 ± 9 cm and 29 ± 12 cm, respectively) remained near-uniform (Fig. 5). Then, flow velocity during deposition of the Qt3, Qt7 and Qt9 alluvium remained nearly uniform. Clast-size

1830
1831
1832
1833 678
1834
1835 679
1836
1837 680
1838
1839 681
1840
1841
1842
1843 682
1844
1845 683
1846
1847 684
1848
1849 685
1850
1851
1852 686
1853
1854 687
1855
1856 688
1857
1858 689
1859
1860
1861 690
1862
1863 691
1864
1865 692
1866
1867
1868 693
1869
1870
1871
1872 694
1873
1874 695
1875
1876 696
1877
1878
1879 697
1880
1881 698
1882
1883 699
1884
1885
1886
1887
1888

averages of the entire set of terraces overlapped within uncertainties. A decrease in the maximum grain size (D_{max}) along each terrace profile has also been observed (Fig. 5), which indicates that the hydraulic shear stress decreases proportionally to the gradient of the stream (Schumm, 1977; Larue, 2008; Pazzaglia, 2013).

The upstream divergence of terrace straths along the Cinca River indicates differential regional uplift as a primary driver of terrace formation rather than changes in fluvial erosivity and incision driven by cycles of climate transition (Whipple et al., 1999; Whipple and Tucker, 1999). Several mechanisms may be involved to explain the postulated differential regional uplift: (i) a reinforced uplift in response to a higher denudation rate affecting the Pyrenees as a function of topographic relief (Champagnac et al., 2008; Stange et al., 2016); (ii) an isostatic rebound of the Central Pyrenees related to lithospheric thickening (Zeyen and Fernández, 1994; Gunnel et al., 2008), supported by an important negative Bouguer anomaly associated with the Pyrenean building (Casas et al., 1997); and (iii) a flexural rebound related to removal of Pleistocene glaciers in the headwaters of the Cinca-Cinqueta valley (Belmonte, 2014).

5.1.3 Migration westward of the Cinca River

The Cinca River has markedly migrated to the west during incision, based on the distribution of mapped terrace surfaces (Fig. 3B, C; Appendix 1). The maximum lateral westward displacement reached 7 km between Qt3 and Qt7 in the Albalate section of the lower Cinca River valley. Westward migration ceased from the Qt7 terrace (61 ± 4 ka). The observed arrangement of the terraces extends to the regional scale because it is common in the Pyrenean side of the central Ebro Basin, as has been shown in the

1889
1890
1891 700 Noguera Ribagorzana River valley (Peña-Monné, 1983; Sancho, 1988), to the east of
1892
1893 the Cinca River, in the Alcanadre River valley (Rodríguez, 1986; Calle et al., 2013), and
1894 701
1895 the Gállego River valley (Benito, 1989), to the west of the Cinca River.
1896 702
1897
1898

1899 703 Lateral migration can play an important role in the river incision rates because it
1900
1901 704 maintains an unconstrained width of the valley over time and, as a consequence, the
1902
1903 obtained river incision rates could be comparable. Fluvial incision into bedrock is
1904 705
1905 basically proportional to the stream power and inversely proportional to the channel
1906 706
1907 width (Howard et al., 1994; Sklar and Dietrich, 1998; Brocard and van der Beek, 2006).
1908 707
1909

1910 708 Terrace treads of the Qt1 to Qt7 terraces consist of wide aggradational surfaces (Figs.
1911
1912 3B, C, 4; Appendix 1). For example, the Qt3 valley section is approximately a minimum
1913 709
1914 of 5.5 km wide at Barbastro and the Qt7 valley width reaches a minimum of 4.5 km at
1915 710
1916 Santa Lecina. Subsequent to formation of the Qt7 terrace, the river valley becomes
1917 711
1918 narrower and the available width to accommodate subsequent terraces decreases
1919 712
1920 (Qt8 and Qt9) to a maximum of 2 km between Monzón and Fraga. Considering the
1921 713
1922 uniform lithology of the geological bedrock (Schanz and Montgomery, 2016), the
1923 714
1924 higher erosivity from Qt7 to Qt9 (the pair Qt7-Qt8 yields a rate of 1.48 m ka^{-1}),
1925 715
1926 therefore, could be, at least partially, related to restrictions imposed by valley width.
1927 716
1928
1929
1930

1931
1932 717 Channel migration and the related asymmetry of Pleistocene terraces may also be
1933
1934 718 controlled by the regional westward tilt of Oligocene-Miocene bedrock in the Ebro
1935
1936 719 basin. Strata dip gently westward (5° maximum) along the western margin of the Cinca
1937
1938 River valley (Sancho, 1988). This regional tilting requires an uplift mechanism more
1939 720
1940 active in eastern Iberia, with tilting related to the uplift of the rift shoulder (including
1941 721
1942 the eastern Pyrenees, the Catalan Coastal Ranges and the adjacent Ebro Basin)
1943 722
1944
1945
1946
1947

(Janssen et al., 1993; Casas-Sainz and de Vicente, 2009) accompanying the opening of the western Mediterranean margin during the Neogene (Roca and Desegaulx, 1992; Coney et al., 1996; Lewis et al., 2000). The uniform altimetry of the sequences of terraces in the main Pyrenean tributaries of the Ebro River, from east to west, however, suggests a cessation of differential uplift in the Mediterranean shoulder from at least the Mid Pleistocene. As a consequence, increased eastern uplift plays an indirect role in the westward migration of the Cinca River through the tilting bedrock.

5.2 Changes in incision rates over the last 1 Ma

Analysis of incision rates indicates that non-uniform river incision in the Cinca River valley has occurred over the last 1 Ma (Table 5; Fig. 8). Temporal changes in fluvial incision rates are particularly well established in the lower reach of the valley where the terrace sequence is preserved. Changes in river incision rates over time can be linked to changes in uplift rates (He et al., 2015; Ruzkiczay-Rüdiger et al., 2016) and/or climate driven changes in erosivity (e.g., Whipple et al., 1999; Schlunegger and Hinderer, 2001; Hartshorn et al., 2002; Zaprowski et al., 2005; Yang et al., 2011).

Using currently available data, there is no evidence of variability in the tectonic uplift rate of NE Iberia during the Mid-Late Pleistocene (Casas-Sainz and de Vicente, 2009; Fernández-Lozano et al., 2011); however, strong variability in climate has been well established, particularly during the Penultimate and the Last Glacial cycles at regional scale (Lewis et al., 2009; Sancho et al., 2015). Lewis et al. (2009) linked fluvial aggradation phases during the Mid-Late Pleistocene in the Cinca River valley with enhanced periods of glacier outwash that produced high discharges of water and

2007
2008
2009 745 sediment yield down-stream along the valley. Therefore, a close correlation was
2010
2011 established between alluvial deposition and cold stages: Qt5 correlates to MIS6, Qt6 to
2012 746
2013 the MIS5b-5c transition, Qt7 to MIS4, Qt8 to the H5 event and Qt9 to the Younger
2014 747
2015 Dryas period (Lewis et al., 2009). Periods of higher fluvial incision would be likely
2016 748
2017 during interstadial stages with a lower sediment supply and greater water discharge
2018 749
2019 activated by retreating glaciers. There is a broad agreement that correlates valley
2020 750
2021 aggradation to cold climates and river incision to transitional and warm climates (e.g.,
2022 751
2023 Chorley et al., 1984; Fuller et al., 1998; Vandenberghe and Maddy, 2001; Macklin et al.,
2024 752
2025 2002; Pan et al., 2003; Vandenberghe, 2003; Gao et al., 2008; Wegmann and Pazzaglia,
2026 753
2027 2009).
2028 754
2029
2030
2031
2032
2033 755 Regional incision also reflects cycles of variable glacial meltwater discharge over time
2034
2035 756 as a function of the extension and retreat of the Cinca and Cinqueta valley glaciers. For
2036
2037 757 example, the last maximum glacier advance in the Central Pyrenees was at 60-70 ka
2038
2039 (MIS4) (Sancho et al., 2003; Lewis et al., 2009) and correlates well with the Qt7 terrace
2040 758
2041 (Lewis et al., 2009), the most important geomorphological marker along the valley. The
2042 759
2043 Cinca-Cinqueta glacier system reached a length of 25 km at this time. Subsequent
2044 760
2045 glacier retreat would produce increased runoff that, in turn, would accelerate fluvial
2046 761
2047 downcutting resulting in higher rates of river incision (Dethier, 2001). As result, the
2048 762
2049 highest expected fluvial incision rates would occur during the timing of the couple Qt7-
2050 763
2051 Qt8 (from 61±4 ka to 47±4 ka) following the last maximum glacier extension. In fact,
2052 764
2053 this is the case; the incision rate was 1.48 m ka⁻¹ in the lower reach of the Cinca River
2054 765
2055 valley (Albalate sector). Nonetheless, the decrease in valley width after Qt7 formation
2056 766
2057
2058
2059
2060
2061
2062
2063
2064
2065

2066
2067
2068
2069
2070
2071
2072
2073
2074
2075
2076
2077
2078
2079
2080
2081
2082
2083
2084
2085
2086
2087
2088
2089
2090
2091
2092
2093
2094
2095
2096
2097
2098
2099
2100
2101
2102
2103
2104
2105
2106
2107
2108
2109
2110
2111
2112
2113
2114
2115
2116
2117
2118
2119
2120
2121
2122
2123
2124

767 must also be considered to explain this high incision rate, as has been previously
768 indicated.

769 The incision rates obtained between Qt6 (97±16 ka) and Qt7 (61±4 ka) formation (0.74
770 m ka⁻¹) and between Qt9 and the active channel (last 11±1 ka) (0.33 m ka⁻¹) are also
771 remarkable. Significantly lower incision rates were deduced during the Mid-
772 Pleistocene (e.g., 0.11 m ka⁻¹ between Qt3 and Qt5 in the Albalate sector), resulting
773 from less intense glacial pulses and/or higher valley width maintained as a
774 consequence of the migration westward of the Cinca River. Our results do not well
775 match the acceleration in river incision during the Mid-Pleistocene Revolution at the
776 global scale (Bridgland and Westaway, 2008). Regardless, the general temporal pattern
777 in the lower reach of the Cinca River valley (Albalate sector) can be extrapolated to the
778 upper reach (Ainsa sector).

779 Finally, agreement between denudation and isostatic rebound must also be considered
780 (Garcia-Castellanos and Lasarrosa, 2015). The increase in fluvial entrenchment would
781 involve a lowering of the regional drainage and an increased denudation between Qt6
782 (97±16 ka) and Qt8 (47±4 ka), which in turn implies a higher erosional isostatic uplift
783 during this period demonstrating a positive feedback loop (Finnegan et al., 2008;
784 Westaway et al., 2009; Schlunegger et al., 2011).

6. Conclusions

785 Incision rates derived from the regional distribution of a well-preserved sequence of
786 staircase terraces along 170 km in the Cinca River valley have been developed for the
787 last 1 Ma in the Central Pyrenees and the adjacent Ebro basin (NE Iberia). The

2125
2126
2127
2128 789
2129
2130 790
2131
2132 791
2133
2134 792
2135
2136 793
2137
2138
2139 794
2140
2141 795
2142
2143
2144 796
2145
2146 797
2147
2148
2149 798
2150
2151 799
2152
2153 800
2154
2155 801
2156
2157
2158 802
2159
2160 803
2161
2162
2163 804
2164
2165 805
2166
2167
2168 806
2169
2170 807
2171
2172 808
2173
2174 809
2175
2176
2177 810
2178
2179 811
2180
2181
2182
2183

sequence is composed of ten well separated terraces (from Qt1 to Qt10) formed under post-orogenic geodynamics and glacial/ interglacial climate conditions. Formation of this extensive paired cyclic terrace sequence was climatically controlled and required a significant regional uplift. Combined results from terrace mapping, height of terrace straths and profiles, and numerical ages of the alluvium overlying terrace straths allow analysis of the spatial and temporal river incision patterns and provides several interpretation of mechanisms involved:

1) Considering coupled successions of the more extensive terraces (Qt3-Qt7, Qt7-Qt9 and Qt9-active channel), the mean fluvial incision rate along the Cinca River during the Middle and Late Pleistocene was approximately around 0.47 m ka^{-1} . This incision rate was slightly greater in the upper reach of the valley (Ainsa sector) (0.56 m ka^{-1}) than in the lower reach (Albalate sector) (0.38 m ka^{-1}). In addition, the highest incision rate (1.48 m ka^{-1}) in the lower reach of the valley occurred during Qt7-Qt8 terrace formation (61-47 ka) and the lowest rate (0.11 m ka^{-1}) occurred during Qt3-Qt5 terrace formation (401-178 ka).

2) The spatial distribution of incision rates showed a near-uniform pattern of fluvial down-cutting along the Cinca River valley. Nearly parallel terrace profiles were driven by a near-uniform regional uplift activated by (i) tectonic uplift related to lithospheric thickening and (ii) isostatic rebound in response to regional denudation unloading, after the connection of the Ebro Basin with the Mediterranean Sea. Subtle upstream divergence of strath profiles appears to be governed by a differential increased uplift in the upper mountainous reach of the valley (Axial Pyrenees) rather than by a decrease in climate-driven erosivity with time.

2184
2185
2186 812 3) Temporal incision rates show a non-uniform time pattern throughout the last 1 Ma.
2187
2188

2189 813 The highest incision rate (1.48 m ka^{-1}) occurred during Qt7-Qt8 terrace formation (61-
2190
2191 814 47 ka). This highest rate appears to be related to a combination of (i) the high glacial
2192
2193 815 meltwater discharge after the last maximum advance of the Pyrenean Cinca-Cinqueta
2194
2195 816 glacier system and (ii) by the deactivation of migration westward of the Cinca River,
2196
2197
2198 817 favouring a lower width of the valley. Currently, the Cinca River is not in equilibrium
2199
2200 818 and modern incision continues.

2201
2202
2203 819 Incision rates calculated in the Ebro Basin draining to the Mediterranean Sea are much
2204
2205 820 higher than rates for the Iberian rivers flowing into the Atlantic Ocean. Undoubtedly,
2206
2207
2208 821 the post-tectonic geodynamic setting of NE Iberia, the denudation triggered after the
2209
2210 822 exorheism of the Ebro basin and the Pleistocene glacier evolution in the Pyrenees play
2211
2212 823 a determinant role in explaining this difference in landscape evolution at the Iberian
2213
2214 824 scale.

2215
2216
2217
2218 825 Additional regional studies of staircase terrace sequences are necessary to validate the
2219
2220 826 proposed spatial and temporal patterns and to confirm the combined effect of uplift
2221
2222 827 and climate on fluvial incision rates and the landscape evolution of NE Iberia.
2223
2224
2225

2226 828 **7. Acknowledgments**

2227
2228
2229 829 This paper is a tribute to Dr. Claudia J. Lewis, who died prematurely when we were
2230
2231 830 developing the manuscript. At the picture, Claudia guiding a field-trip to the Cinca
2232
2233 831 River Valley included in the program of the V Spanish Geological Congress (2004). The
2234
2235
2236 832 paper collects much of the hard work performed cooperatively between 1998 and
2237
2238 833 2012. Research was funded by grants from the National Geographic Society, the
2239
2240
2241
2242

2243
2244
2245 834 National Science Foundation (EAR-0088714), U.S. Army Research Office grants
2246
2247
2248 835 DAAD19-03-1-0159 and W911NF-09-1-0256, the Spanish Ministry of Education, and a
2249
2250 836 Fulbright Senior Scholar grant to C. Lewis. We thank the Institute of Geophysics and
2251
2252 837 Planetary Physics and Laboratory Directed Research and Development (LDRD) at Los
2253
2254 838 Alamos National Laboratory for additional funding. The Desert Research Institute
2255
2256
2257 839 provided GPS equipment. Laboratory soil analyses were carried out at the Desert
2258
2259 840 Research Institute. We thank John Geissman, Bet Beamud and Miguel Garcés for use of
2260
2261 841 the paleomagnetic labs at the University of New Mexico (Albuquerque) and the
2262
2263 842 Institute of Earth Sciences “Jaume Almera” CSIC-UB (Barcelona, Spain). We thank
2264
2265
2266 843 Marta Lopez for combining all of our data into a Geographic Information System. This
2267
2268 844 study is a contribution of the PALEOQ Research Group (Aragon Government and
2269
2270 845 European Social Fund) and IUCA (University of Zaragoza). Authors thank two
2271
2272 846 anonymous reviewers for their comments that helped improve the manuscript. Thanks
2273
2274
2275 847 are also due to the Editor Prof. Andy Plater for the final refinement of the manuscript.
2276
2277

2278 848 **References**

2279
2280
2281 849 Antón, L., Rodés, A., De Vicente, G., Pallàs, R, Garcia-Castellanos, D., Stuart, F.M.,
2282
2283 850 Braucher, R. and Bourlès, D. (2012). Quantification of fluvial incision in the Duero Basin
2284
2285
2286 851 (NW Iberia) from longitudinal profile analysis and terrestrial cosmogenic nuclide
2287
2288 852 concentrations. *Geomorphology*, 165-166, 50-61.
2289
2290
2291 853 Bailey, R.C. and Halls, H.C. (1984). Estimate of confidence in paleomagnetic directions
2292
2293
2294 854 derived from mixed remagnetization circle and direct observational data. *Journal of*
2295
2296 855 *Geophysics*, 54, 174-182.
2297
2298
2299
2300
2301

2302
2303
2304 856 Barnolas, A., Gil-Peña, I. and Martín-Alfageme, S. (2009). Mapa Geológico de Pirineos a
2305
2306 escala 1:400.000. IGME-BRGM.
2307 857
2308
2309
2310 858 Belmonte, A. (2014). Geomorfología del Macizo de Cotiella (Pirineo oscense):
2311
2312 859 Cartografía, evolución paleoambiental y dinámica actual. PhD thesis, University of
2313
2314 860 Zaragoza, 580 p.
2315
2316
2317
2318 861 Beltrán, A. (1985). Historia de Aragón, vol. II. Guara Editorial, 183 p. Zaragoza.
2319
2320
2321 862 Benito, G. (1989). Geomorfología de la Cuenca Baja del río Gállego. PhD thesis,
2322
2323 863 University of Zaragoza, 764 p.
2324
2325
2326
2327 864 Benito, G., Sancho, C., Peña, J.L., Machado, M.J. and Rhodes, E.J. (2010). Large-scale
2328
2329 865 karst subsidence and accelerated fluvial aggradation during MIS6 in NE Spain: climatic
2330
2331 866 and paleohydrological implications. Quaternary Science Reviews, 29, 2694-2704.
2332
2333
2334
2335 867 Birkeland, P.W. (1999). Soils and Geomorphology. Oxford University Press, New York.
2336
2337 868 430 p.
2338
2339
2340 869 Bridgland, D.R. (2000). River terrace systems in north-west Europe: an archive of
2341
2342 870 environmental change, uplift and early human occupation. Quaternary Science
2343
2344
2345 871 Reviews, 19, 1293-1303.
2346
2347
2348 872 Bridgland, D. and Westaway, R. (2008). Climatically controlled river terrace staircases:
2349
2350 873 A worldwide Quaternary phenomenon. Geomorphology , 98, 285-315.
2351
2352
2353
2354 874 Brocard, G.Y. and van der Beek, P.A. (2006). Influence of incision rate, rock strength,
2355
2356 875 and bedload supply on bedrock river gradients and valley-flat widths: field-based
2357
2358
2359
2360

2361
2362
2363 876 evidence and calibrations from western Alpine rivers (southeast France). In Willet, S.D.,
2364
2365 Hovious, N., Brandon, M.T. and Fisher, D.M. (Eds.). Tectonics, Climate and Landscape
2366 877 Evolution. Geological Society of America, Special Paper 398, 101-126.
2367
2368 878
2369
2370
2371 879 Bull, W.B. (1991). Geomorphic Response to Climatic Change. Oxford University Press,
2372
2373 880 326 p. New York.
2374
2375
2376
2377 881 Burbank, D.W. and Anderson, R.S. (2001). Tectonic Geomorphology. Blackwell, 274
2378
2379 882 Malden.
2380
2381
2382 883 Calle, M., Sancho, C., Peña, J.L., Cunha, P., Oliva-Urcia, B. and Pueyo, E. (2013). La
2383
2384 884 secuencia de terrazas cuaternarias del río Alcanadre (provincia de Huesca):
2385
2386 885 caracterización y consideraciones paleoambientales. Cuadernos de Investigación
2387
2388 886 Geográfica, 39, 159-178.
2389
2390
2391
2392 887 Casas, A., Kearey, P., Rivero, L. and Adam, C.R. (1997). Gravity anomaly map of the
2393
2394 888 Pyrenean region and a comparison of the deep geological structure of the western and
2395
2396 889 eastern Pyrenees. Earth and Planetary Science Letters, 150, 65-78.
2397
2398
2399
2400 890 Casas-Sainz, A.M. and de Vicente, G. (2009). On the tectonic origin of Iberian
2401
2402 891 topography. Tectonophysics, 474, 214-235.
2403
2404
2405
2406 892 Champagnac, J.D., van der Beek, P., Diraison, G. and Dauphin, S. (2008). Flexural
2407
2408 893 isostatic response of the Alps to increased Quaternary erosion recorded by foreland
2409
2410 894 basin remnants, SE France. Terra Nova, 20, 213-220.
2411
2412
2413
2414 895 Chorley, R.J., Schumm, S.A. and Sugden, D.E. (1984). Geomorphology. Methuen, 605 p.
2415
2416 896 London.
2417
2418
2419

2420
2421
2422
2423 897 Cloetingh, S. and Willett, S.D. (2013). TOPO-EUROPE: Understanding of the coupling
2424 between the deep Earth and continental topography. *Tectonophysics*, 602, 1-14.
2425 898
2426
2427
2428 899 Cloetingh, S., Burov, E., Beekman, F., Andeweg, B., Andriessen, P.A.M., Garcia-
2429
2430 900 Castellanos, D., de Vicente, G. and Vegas, R. (2002). Lithospheric folding in Iberia.
2431
2432 Tectonics, 21, 5-1-5-26.
2433 901
2434
2435
2436 902 Coney, P.J., Muñoz, J.A., McClay, K.R. and Evenchick, C.A. (1996). Syntectonic burial
2437
2438 903 and post-tectonic exhumation of the southern Pyrenees foreland fold-and-thrust belt.
2439
2440 904 *Journal of the Geological Society, London*, 153, 9-16.
2441
2442
2443
2444 905 Costa, E., Garcés, M., López-Blanco, M., Beamud, E., Gómez-Paccard, M. and
2445
2446 906 Larrasoaña, J.C. (2010). Closing and continentalization of the South Pyrenean foreland
2447
2448 907 basin (NE Spain): magnetochronological constraints. *Basin Research*, 26, 904-917.
2449
2450
2451 908 Cunha, P.P., Martins, A.A., Daveau, S., Friend, P. (2005). Tectonic control of the Tejo
2452
2453 river fluvial incision during the late Cenozoic, in Ródão-central Portugal (Atlantic
2454 909 Iberian border). *Geomorphology*, 64, 271-298.
2455
2456 910
2457
2458
2459 911 Cunha, P.P., Martins, A.A., Huot, S., Murray, A.S. and Raposo, L. (2008). Dating the Tejo
2460
2461 912 river lower terraces in the Ródão area (Portugal) to assess the role of tectonics and
2462
2463 uplift. *Geomorphology*, 102, 43-54.
2464 913
2465
2466
2467 914 Cunha, P.P., Almeida, N., Aubry, T., Martins, A.A., Murray, S.A., Buylaert, J.P., Sohbaty,
2468
2469 915 R., Raposo, L. and Rocha, L. (2012). Records of human occupation from Pleistocene
2470
2471 river terrace and aeolian sediments in the Arneiro depression (Lower Tejo River,
2472 916
2473 central eastern Portugal). *Geomorphology*, 165-166, 78-90.
2474 917
2475
2476
2477
2478

2479
2480
2481 918 Dethier, D.P. (2001). Pleistocene incision rates in the western United States calibrated
2482 using lava Creek B tephra. *Geology*, 29, 783-786.
2483
2484 919
2485
2486
2487 920 Dubar, M. and Semah, F. (1986). Paleomagnetic data bearing on the age of high terrace
2488 deposits (Durance Sequence) in Alpine valleys of southeastern France. *Quaternary*
2489 921
2490 *Research*, 25, 387-391.
2491 922
2492
2493
2494
2495 923 Duval, M., Sancho, C., Calle, M., Guilarte, V. and Peña-Monné, J.L. (2015). On the
2496 potential of the ESR dating method applied to optically bleached quartz grains in
2497 924
2498 sedimentary fluvial environments: some examples from the Early Pleistocene terraces
2499 925
2500 of the Alcanadre river (Ebro basin, Spain). *Quaternary Geochronology*, 29, 58-69.
2501 926
2502
2503
2504
2505 927 Fernández-Lozano, J., Sokoutis, D., Willingshofer, E., Muñoz-Martín, A., De Vicente, G.
2506 and Cloetingh, S., (2011). Análisis integrado de la topografía y anomalías gravimétricas
2507 928
2508 en la Península Ibérica: nuevas metodologías en modelación análoga. *Revista de la*
2509 929
2510 *Sociedad Geológica de España*, 24, 153-171.
2511 930
2512
2513
2514
2515 931 Finnegan, N.J., Hallet, B., Montgomery, D.R., Zeitler, P.K., Stone, J.O., Anders, A.M. and
2516 Yuping, L. (2008). Coupling of rock uplift and river incision in the Namche Barwa-Gyala
2517 932
2518 Peri massif, Tibet. *Geological Society of America Bulletin*, 120, 142-155.
2519 933
2520
2521
2522
2523 934 Fisher, R. (1953). Dispersion on a sphere. *Proceedings of the Royal Society of London.*
2524 *Series A. Mathematical and Physical Sciences*, 217, 295-305.
2525 935
2526
2527
2528 936 Fitzgerald, P.G., Muñoz, J.A., Coney, P.J. and Baldwin, S.L. (1999). Asymmetric
2529 exhumation across the Pyrenean orogen: implications for the tectonic evolution of a
2530
2531 937
2532 collisional orogen. *Earth and Planetary Science Letters*, 173, 157-170.
2533 938
2534
2535
2536
2537

2538
2539
2540
2541 939 Fuller, I.C., Macklin, M.G., Lewin, J., Passmore, D.G. and Wintle, A.G. (1998). River
2542 response to high-frequency climate oscillations in southern Europe over the past 200
2543 940 k.y. *Geology*, 26, 275-278.
2544
2545 941
2546
2547
2548 942 Gao, H., Liu, X., Pan, B., Wang, Y., Yu, Y. and Li, J. (2008). Stream response to
2549 Quaternary tectonic and climatic change: Evidence from the upper Weihe River,
2550 943 central China. *Quaternary International*, 186, 123-131.
2551
2552
2553 944
2554
2555
2556 945 Garcia-Castellanos, D., Vergés, J., Gaspar-Escribano, J. and Cloetingh, S. (2003).
2557 Interplay between tectonics, climate, and fluvial transport during the Cenozoic
2558 946 evolution of the Ebro Basin (NE Iberia). *Journal of Geophysical Research*, 108, 2347,
2559 doi:10.1029/2002JB002073.
2560
2561 947
2562
2563 948
2564
2565
2566 949 Garcia-Castellanos, D. and Larrasoaña, J.C. (2015). Quantifying the post-tectonic
2567 topographic evolution of closed basins: The Ebro basin (northeast Iberia). *Geology*,
2568 950 43, 663-666.
2569
2570
2571 951
2572
2573
2574 952 García-Ruiz, J.M., Martí-Bono, C., Peña-Monné, J.L., Sancho, C., Rhodes, E.J., Valero-
2575 Garcés, B., González-Sampériz, P. and Moreno, A. (2013). Glacial and fluvial deposits in
2576 953 the Aragón Valley, central-western Pyrenees: chronology of the Pyrenean late
2577 Pleistocene glaciers. *Geografiska Annaler: Series A, Physical Geography*, 95, 15-32.
2578 954
2579
2580
2581 955
2582
2583
2584 956 Gaspar-Escribano, J. M., van Wees, J. D., ter Voorde, M., Cloetingh, S., Roca, E.,
2585 Cabrera, L., Muñoz, J. A., Ziegler, P. A. and Garcia-Castellanos, D. (2001). Three-
2586 957 dimensional flexural modelling of the Ebro Basin (NE Iberia). *Geophysical Journal
2587 International*, 145, 349-367.
2588 958
2589
2590
2591 959
2592
2593
2594
2595
2596

2597
2598
2599 960 Giachetta, E., Molin, P., Scotti, V.N. and Faccena, C. (2015). Plio-Quaternary uplift of
2600
2601 the Iberian Chanin (central-eastern Spain) from landscape evolution experiments and
2602 961
2603 river profile modeling. *Geomorphology*, 246, 48-67.
2604 962
2605
2606
2607 963 Gibbard, P. and Cohen, K.M. (2008). Global chronostratigraphical correlation table for
2608
2609 the last 2.7 million years. *Episodes*, 31, 243-247.
2610 964
2611
2612
2613 965 Gibbard, P.L. and Lewin, J. (2009). River incision and terrace formation in the late
2614
2615 Cenozoic of Europe. *Tectonophysics* 474, 41-55.
2616
2617
2618 967 Gibson, M., Sinclair, H.D., Lynn, G.J. and Stuart, F.M. (2007). Late- to post-orogenic
2619
2620 exhumation of the Central Pyrenees revealed through combined thermochronological
2621 968
2622 data and modeling. *Basin Research*, 19, 323-334.
2623 969
2624
2625
2626 970 Gil Garbi, H, 2017. Los depósitos cuaternarios en el sector central de la Cuenca del
2627
2628 Ebro: Arquitectura sedimentaria, paleokarst, su interacción con la sedimentación y
2629 971
2630 cronología. PhD thesis, University of Zaragoza, 354 p.
2631 972
2632
2633
2634 973 Gil, H., Luzón, A., Soriano, M.A., Casado, I., Pérez, A., Yuste, A., Pueyo, E.L. and Pocoví,
2635
2636 A. (2013). Stratigraphic architecture of alluvial-aeolian systems developed on active
2637 974
2638 karst terrains: an Early Pleistocene example from the Ebro Basin (NE Spain).
2639 975
2640
2641 976 *Sedimentary Geology*, 296, 122-141.
2642
2643
2644 977 Gile, L.H., Hawley, J.H. and Grossman, R.B. (1981). Soils and geomorphology in the
2645
2646 basin and range area of Southern New Mexico-guidebook to the desert project. New
2647 978
2648 Mexico Bureau of Mines and Mineral Resources, Socorro, NM. Memoir 39, 222 p.
2649 979
2650
2651
2652
2653
2654
2655

2656
2657
2658
2659 980 Gunnell, Y., Zeyen, H. and Calvet, M. (2008). Geophysical evidence of a missing
2660 lithospheric root beneath the Eastern Pyrenees: Consequences for post-orogenic uplift
2661 981 and associated geomorphic signatures. *Earth and Planetary Science Letters*, 276, 302-
2662 313.
2663 982
2664
2665 983
2666
2667
2668 984 Gutiérrez, M. and Peña, J.L. (1994). Depresión del Ebro. In Gutiérrez, M. (Ed.).
2669 Geomorfología de España, 305-349. Ed. Rueda. Madrid.
2670
2671 985
2672
2673
2674 986 Hack, J.T. (1973). Stream-profile analysis and stream-gradient index. *Journal Research*
2675 U.S. Geological Survey, 1, 421-429.
2676 987
2677
2678
2679
2680 988 Harden, J.W. (1982). A quantitative index of soil development from field descriptions:
2681 examples from a soil chronosequence in central California. *Geoderma*, 28, 1-28.
2682 989
2683
2684
2685 990 Harden, J.W. and Taylor, E.M. (1983). A quantitative comparison of soil development in
2686 four climatic regimes. *Quaternary Research*, 20, 342-359.
2687 991
2688
2689
2690
2691 992 Hartshorn, K., Hovius, N., Dade, W.B. and Slingerland, R.L. (2002). Climate-driven
2692 bedrock incision in an active mountain belt. *Science*, 297, 2036-2038.
2693 993
2694
2695
2696 994 He, Z., Zhang, X., Bao, S., Qiao, Y., Sheng, Y., Liu, X., He, X., Yang, X., Zhao, J., Liu, R. and
2697 Lu, C. (2015). Multiple climatic cycles imprinted on regional uplift-controlled fluvial
2698 terraces in the lower Yalong River and Anning River, SE Tibetan Plateau.
2699 995
2700
2701 996
2702
2703 997
2704
2705
2706 998 Howard, A.D., Dietrich, W.E. and Seidl, M.A. (1994). Modeling fluvial erosion on
2707 regional to continental scales. *Journal of Geophysical Research* 99 (B7), 13,971-13,986.
2708
2709 999
2710
2711
2712
2713
2714

2715
2716
2717
1000 Jacobson, R.B., Elston, D. P. and Heaton, J.W. (1988). Stratigraphy and magnetic
2718
2719 polarity of the high terrace remnants in the upper Ohio and Monongahela rivers in
2720 1001
2721 West Virginia, Pennsylvania, and Ohio. *Quaternary Research*, 29, 216-232.
2722 1002
2723
2724
2725 1003 Janssen, M.E., Torné, M., Cloetingh, S. and Banda, E. (1993). Pliocene uplift of the
2726
2727 eastern Iberian margin: inferences from quantitative modelling of the Valencia Trough.
2728 1004
2729 Earth and Planetary Science Letters, 119, 585-597.
2730 1005
2731
2732
2733 1006 Kirschvink, J.L. (1980). The least-squares line and plane and the analysis of
2734
2735 palaeomagnetic data. *Geophysical Journal of the Royal Astronomical Society*, 62, 699-
2736 1007
2737 718.
2738 1008
2739
2740
2741 1009 Larue, J.P. (2008). Tectonic influence on the Quaternary drainage evolution on the
2742
2743 northwestern margin of the French Central Massif: the Cruese valley example.
2744 1010
2745 Geomorphology, 93, 398-420.
2746 1011
2747
2748
2749 1012 Lewis, C., McDonald, E., Sancho, C., Peña, J.L. and Rhodes, E. (2009). Climatic
2750
2751 implications of correlated Upper Pleistocene glacial and fluvial deposits on the Cinca
2752 1013
2753 and Gállego Rivers (NE Spain) based on OSL dating and soil stratigraphy. *Global and*
2754 1014
2755 *Planetary Change*, 67, 141-152.
2756 1015
2757
2758
2759 1016 Lewis, C.J., Vergés, J. and Marzo, M. (2000). High mountains in a zone of extended
2760
2761 crust: Insights into the Neogene-Quaternary topographic development of northeastern
2762 1017
2763 Iberia. *Tectonics*, 19, 86-102.
2764 1018
2765
2766
2767 1019 Li, J.J., Fang, X.M., van der Voo, R., Zhu, J.J., Mac Niocaill, C., Ono, Y., Pan, B.T., Zhong,
2768
2769 W., Wang, J.L., Sasaki, T., Zhang, Y.T, Cao, J.X., Kang, S.C. and Wang, J.M. (1997).
2770 1020
2771
2772
2773

2774
2775
2776
1021 Magnetostratigraphic dating of river terraces: Rapid and intermittent incision by the
2777
2778 Yellow River of the northeastern margin of the Tibetan Plateau during the Quaternary.
2779
2780
2781 1023 Journal of Geophysical Research, 102, 10121-10132.
2782
2783
2784
1024 Lucha, P., Gutiérrez, F. and Guerrero, J. (2008). Environmental problems and geological
2785
2786 implications derived from evaporite dissolution in the Barbastro salt anticline (NE
2787
2788 Spain). Environmental Geology, 53, 1045-1055.
2789
2790
2791
2792
1027 Macklin, M.G., Fuller, I.C., Lewin, J., Maas, G.S., Passmore, D.G., Rose, J., Woodward,
2793
2794 J.C., Black, S., Hamlin, R.H.B. and Rowan, J.S. (2002). Correlation of fluvial sequences in
2795
2796 the Mediterranean basin over the last 200 ka and their relationship to climate change.
2797
1029 Quaternary Science Reviews, 21, 1633-1641.
2798
2799
2800
2801
2802
1031 Martínez-Peña, M. and Casas-Sainz, A. (2003). Cretaceous-Tertiary tectonic inversion
2803
2804 of the Cotiella Basin (southern Pyrenees, Spain). International Journal of Earth
2805
2806 Sciences, 92, 99-113.
2807
1033
2808
2809
2810
1034 Martínez-Peña, B., Casas-Sainz, A. and Millán-Garrido, H. (1995). Palaeostresses
2811
2812 associated with thrust sheet emplacement and related holding folding in the southern
2813
2814 central Pyrennes, Huesca, Spain. Journal of the Geological Society, London, 152, 353-
2815
1036 364.
2816
2817
1037
2818
2819
2820
1038 Martins, A.A., Cunha, P.P., Huot, S., Murray, A.S. and Buylaert, J.P. (2009).
2821
2822 Geomorphological correlation of the tectonically displaced Tejo River terraces
2823
2824 (Gavião–Chamusca area, central Portugal) supported by luminescence dating.
2825
1040 Quaternary International, 199, 75-91.
2826
2827
1041
2828
2829
2830
2831
2832

2833
2834
2835
1042 Martins, A.A., Cunha, P.P., Buylaert, J.P., Huot, S., Murray, A.S., Dinis, P., Stokes, M.
2836
2837 (2010). K-feldspar IRSL dating of a Pleistocene river terrace sequence of the Lower Tejo
2838
2839 River (Portugal, western Iberia). *Quaternary Geochronology*, 5, 176-180.
2840
2841
2842
2843
1045 McDonald, E.V., Reneau, S.L. and Gardner, J.N. (1996). Soil-forming processes on the
2844
2845 Pajarito Plateau: Investigation of a soil chronosequence in Rendija Canyon. In: Goff, F.,
2846
1046 Kues, B.S., Rogers, M.A., McFadden, L.D. and Gardner, J.N. (Eds.), New Mexico
2847
2848 Geological Society Guidebook, 47th Conference. Socorro, New Mexico, USA, p. 375-
2849
2850
1048
2851
2852
1049 382.
2853
2854
2855
1050 Merritts, J., Vicent, R. and Wohl, E. (1994). Long river profiles, tectonism and eustasy: a
2856
2857
1051 guide to interpreting fluvial terraces. *Journal of Geophysical Research* 99 (B7), 14031-
2858
2859
1052 14050.
2860
2861
2862
2863
1053 Miall, A.D. (1978). Lithofacies types and vertical profile models in braided river
2864
2865
1054 deposits: a summary. In: Miall, A.D. (Ed.). *Fluvial sedimentology*. Canadian Society of
2866
2867
1055 Petroleum Geologists, Memoir 5, 597-604.
2868
2869
2870
2871
1056 Moreno, D., Falguères, C., Pérez-González, A., Duval, M., Voinchet, P., Benito-Calvo, A.,
2872
2873
1057 Ortega, A.I., Bahain, J.J., Sala, R., Carbonell, E., Bermúdez de Castro, J.M. and Arsuaga,
2874
2875
1058 J.L. (2012). ESR chronology of alluvial deposits in the Arlanzón valley (Atapuerca,
2876
2877
1059 Spain): Contemporaneity with Atapuerca Gran Dolina site. *Quaternary Geochronology*,
2878
2879
1060 10, 418-423.
2880
2881
2882
2883
1061 Muñoz, J.A. (2002). The Pyrenees. In Gibbons, W. and Moreno, M.T. (Eds.). *The*
2884
2885
1062 *Geology of Spain*, 370-385. Geological Society, London.
2886
2887
2888
2889
2890
2891

2892
2893
2894
1063 Muñoz, A., Arenas, C., González, A., Luzón, A., Pardo, G., Pérez, A. and Villena, J.
2895
2896
1064 (2002). Ebro basin (northeastern Spain). In Gibbons, W. and Moreno, M.T. (Eds.). The
2897
2898
1065 Geology of Spain, 301-309. Geological Society, London.
2899
2900
2901
2902
1066 Pan, B.T., Burbank, D., Wang, Y.X., Wu, G.J., Li, J.J. and Guan, Q.Y. (2003). A 900 ka
2903
2904
1067 record of strath terrace formation during glacial-interglacial transitions in northwest
2905
2906
1068 China. *Geology*, 31, 957-960.
2907
2908
2909
1069 Pazzaglia, F.J. (2013). Fluvial Terraces. In Wohl, E. (Ed.). *Treatise of Geomorphology*,
2910
2911
1070 Volume 9, 379-412. Elsevier.
2912
2913
2914
2915
1071 Pazzaglia, F.J. and Brandon, M.T. (2001). A fluvial record of rock uplift and shortening
2916
2917
1072 across the Cascadia forearc high. *American Journal of Science*, 301, 385-431.
2918
2919
2920
2921
1073 Peña-Monné, J.L. (1983). La Conca de Tremp y Sierras Prepirenaicas comprendidas
2922
2923
1074 entre los ríos Segre y Noguera Ribagorzana: estudio geomorfológico. Instituto de
2924
2925
1075 Estudios Ilerdenses, 373 p., Lleida.
2926
2927
2928
2929
1076 Peña-Monné, J.L. (1994). Cordillera Pirenaica. In Gutiérrez, M. (Ed.). *Geomorfología de*
2930
2931
1077 *España*, 159-225. Rueda, Madrid.
2932
2933
2934
1078 Pérez-Rivarés, J., Garcés, M., Arenas, C. and Pardo, G. (2002). Magnetocronología de la
2935
2936
1079 sucesión Miocena de la Sierra de Alcubierre (sector central de la Cuenca del Ebro).
2937
2938
1080 *Revista Sociedad Geológica de España*, 15, 3-4.
2939
2940
2941
2942
1081 Pevzner, M.A. (1970). Paleomagnetic studies of Pliocene-Quaternary deposits of
2943
2944
1082 Pridniestrovie. *Palaeogeography, Palaeoclimatology, Palaeoecology*, 8, 215-219.
2945
2946
2947
2948
2949
2950

2951
2952
2953
1083 Pueyo, E.L., Garcés, M., Mauritsch, H.J., Lewis, C., Scholger, R., Sancho, C., Molina, R.,
2954
2955
1084 Schnepf, E., Larrasoña, J.C., Parés, J.M., Pocoví, A., Muñoz, A., Valero, B., Millán, H.,
2956
2957
1085 Laplana, C., Oliva, B. and González, P. (2006). Sampling, transportation and magnetic-
2958
2959
1086 free consolidation of extremely soft sediments for paleomagnetic purposes: a
2960
2961
1087 successful "recipe". In Calvo, M., Garcés, M., Gomes, C., Larrasoña, J.C., Pueyo, E. and
2962
2963
1088 Villalaín, J.J. (Eds). MAGIBER I: Paleomagnetismo en la Península Ibérica, 121-128.
2964
2965
1089 Universidad de Burgos, ISBN: 84-96394-35-2.
2966
2967
2968
2969
1090 Puigdefábregas, C. and Souquet, P. (1986). Tecto-sedimentary cycles and depositional
2970
2971
1091 sequences of the Mesozoic and Tertiary from the Pyrenees. In Banda, E. and Wickham,
2972
2973
1092 S.M. (Eds.). The Geological Evolution of the Pyrenees, Tectonophysics, 129, 173-203.
2974
2975
2976
2977
1093 Ramón, M.J., Pueyo, E.L., Oliva-Urcia, B. and Larrasoña, J.C. (2017). Virtual Directions
2978
2979
1094 in Paleomagnetism: A Global and Rapid Approach to Evaluate the NRM Components.
2980
2981
1095 Frontiers of Earth Science, 5, 1-14.
2982
2983
2984
2985
1096 Roca, E. and Desegaulx, P. (1992). Analysis of the geological evolution and vertical
2986
2987
1097 movements in the València trough area, western Mediterranean. Marine and
2988
2989
1098 Petroleum Geology, 9, 167-185.
2990
2991
2992
2993
1099 Rodríguez, J. (1986). Geomorfología de las Sierras Exteriores oscenses y su
2994
2995
1100 piedemonte. Instituto de Estudios Altoaragoneses, Huesca, 172 p.
2996
2997
2998
2999
1101 Ruskiczay-Rüdiger, Z., Braucher, R., Novothny, A., Csillag, G., Fodor, L., Molnár, G.,
3000
3001
1102 Madarász, B. and ASTER Team (2016). Tectonic and climatic control on terrace
3002
3003
1103 formation: Coupling in situ produced ¹⁰Be depth profiles and luminescence approach,
3004
3005
1104 Danube River, Hungary, Central Europe. Quaternary Science Reviews, 131, 127-147.
3006
3007
3008
3009

3010
3011
3012
1105 Sancho, C. (1988). Geomorfología de la cuenca baja del río Cinca. PhD thesis, University
3013
3014
1106 of Zaragoza, 743 p.
3015
3016
3017
1107 Sancho, C. (1989). Deformaciones asociadas a la actividad diapírica cuaternaria del
3018
3019
1108 Anticlinal de Barbastro (provincia de Huesca). Cuaternario y Geomorfología, 3, 35-43.
3020
3021
3022
1109 Sancho, C., Calle, M., Peña-Monné, J.L., Duval, M., Oliva-Urcia, B., Pueyo, E.L., Benito,
3023
3024
1110 G. and Moreno, A. (2016). Dating the earliest Pleistocene alluvial terrace of the
3025
3026
1111 Alcanadre River: Insights on the landscape evolution of the Ebro Basin (NE Spain).
3027
3028
1112 Quaternary International, 407, 86-95.
3029
3030
3031
3032
3033
1113 Sancho, C., Peña, J.L., Lewis, C., McDonald, E. and Rhodes, E. (2003). Preliminary dating
3034
3035
1114 of glacial and fluvial deposits in the Cinca River Valley (NE Spain): chronological
3036
3037
1115 evidences for the Glacial Maximum in the Pyrenees?. In Ruiz, M.B., Dorado, M.,
3038
3039
1116 Valdeolmillos, A., Gil, M.J., Bardají, T., Bustamante, I. and Martínez, I. (Eds.).
3040
3041
1117 Quaternary climatic changes and environmental crises in the Mediterranean region,
3042
3043
1118 169-173. Universidad de Alcalá-Ministerio de Ciencia y Tecnología-INQUA.
3044
3045
3046
3047
1119 Sancho, C., Arenas, C., Vázquez-Urbez, M., Pardo, G., Lozano, M.V., Peña-Monné, J.L.,
3048
3049
1120 Hellstrom, J., Ortiz, J.E., Osácar, M.C., Auqué, L. and Torres, T. (2015). Climatic
3050
3051
1121 implications of the Quaternary fluvial tufa record in the NE Iberian Peninsula over the
3052
3053
1122 last 500 ka. Quaternary Research, 84, 398-414.
3054
3055
3056
3057
1123 Santisteban, J. I. and Schulte, L. (2007). Fluvial networks of the Iberian Peninsula: a
3058
3059
1124 chronological framework. Quaternary Science Reviews, 26, 2738-2757.
3060
3061
3062
3063
3064
3065
3066
3067
3068

3069
3070
3071 1125 Schanz, S.A. and Montgomery, D.R. (2016). Lithologic controls on valley width and
3072
3073 strath terrace formation. *Geomorphology*, 258, 58-68.
3074 1126
3075
3076
3077 1127 Scheepers, P.J.J. and Zijdeveld, J.D.A. (1992). Stacking in Paleomagnetism: Application
3078
3079 1128 to marine sediments with weak NRM, *Geophysical Research Letters*, 19, 1519-1522.
3080
3081
3082 1129 Schlunegger, F. and Hinderer, M. (2001). Crustal uplift in the Alps: why the drainage
3083
3084 pattern matters. *Terra Nova*, 13, 425-432.
3085 1130
3086
3087
3088 1131 Schlunegger, F., Norton, K.P. and Zeilinger, G. (2011). Climatic forcing on channel
3089
3090 1132 profiles in the Eastern Cordillera on the Coroico region, Bolivia. *The Journal of Geology*,
3091
3092 1133 119, 97-107.
3093
3094
3095
3096 1134 Schumm, S.A. (1977). *The fluvial system*. John Wiley & Sons, 338 p. New York.
3097
3098
3099 1135 Scotti, V.N., Molin, P., Faccenna, C., Soligo, M. and Casas-Sainz, A. (2014). The influence
3100
3101 1136 of surface and tectonic processes on landscape evolution of the Iberian Chain (Spain):
3102
3103 quantitative geomorphological analysis and geochronology. *Geomorphology*, 206, 37-
3104 1137 57.
3105
3106 1138
3107
3108
3109 1139 Sklar, L. and Dietrich, W.E. (1998). River longitudinal profiles and bedrock incision
3110
3111 models: stream power and the influence of sediment supply. In: Tinkler, K.J. and Wohl,
3112 1140 E.E. (Eds.). *Rivers Over Rock: Fluvial Processes in Bedrock Channels*. Geophysical
3113
3114 1141 Monograph, 107. American Geophysical Union, 237-260. Washington D.C.
3115
3116 1142
3117
3118
3119 1143 Silva, P.G., Roquero, E., López-Recio, M., Huerta, P. and Tapias, F. (2013). Statistical
3120
3121 approach to the chronosequence of fluvial terraces in the Tagus and Duero basins
3122 1144
3123
3124
3125
3126
3127

3128
3129
3130
3131 1145 (Central Spain). In: Baena, R., Fernández, J.J. and Guerrero, I. (Eds.). El Cuaternario
3132 Ibérico: Investigación en el S. XXI, 29-33. Sevilla.
3133 1146
3134
3135
3136 1147 Silva, P.G., Roquero, E., López-Recio, M., Huerta, P. and Martínez-Graña, A.M. (2016).
3137
3138 1148 Chronology of fluvial terrace sequences for large Atlantic rivers in the Iberian Peninsula
3139
3140 (Upper Tagus and Duero drainage basins, Central Spain). Quaternary Science Reviews
3141
3142 doi.org/10.1016/j.quascirev.2016.05.027.
3143 1150
3144
3145
3146 1151 Singer, B.S. (2014). A Quaternary geomagnetic instability time scale. Quaternary
3147
3148 1152 Geochronology, 21, 29-52.
3149
3150
3151
3152 1153 Soria-Jáuregui, A., González-Amuchástegui, M.J., Mauz, B. and Lang, A. (2016).
3153
3154 1154 Dynamics of Mediterranean late Quaternary fluvial activity: An example from the River
3155
3156 1155 Ebro (north Iberian Peninsula). Geomorphology, 268, 110-122.
3157
3158
3159
3160 1156 Stange, K.M., van Balen, R., Vandenberghe, J., Peña, J.L. and Sancho, C. (2013). External
3161
3162 1157 controls on Quaternary fluvial incision and terrace formation at the Segre River,
3163
3164 1158 Southern Pyrenees. Tectonophysics, 602, 316-331.
3165
3166
3167 1159 Stange, K.M., van Balen, R.T., Garcia-Castellanos, D., Cloetingh, S. (2016). Numerical
3168
3169 1160 modelling of Quaternary terrace staircase formation in the Ebro foreland basin,
3170
3171 southern Pyrenees, NE Iberia. Basin Research, 28, 124-146.
3172 1161
3173
3174
3175 1162 Starkel, L. (2003). Climatically controlled terraces in uplifting mountain areas.
3176
3177 1163 Quaternary Science Reviews, 22, 2189-2198.
3178
3179
3180
3181 1164 Stokes, M., Cunha, P.P. and Martins, A. (2012). Techniques for analysing Late Cenozoic
3182
3183 1165 river terrace sequences. Geomorphology, 165, 1-6.
3184
3185
3186

3187
3188
3189
3190 1166 U.S. Soil Survey Staff (1993). Examination and description of soils. Soil Conservation
3191 Service. Soil survey manual. U.S. Department of Agriculture Handbook 18. Washington,
3192 1167
3193 D.C., USA, Chapter 3.
3194 1168
3195
3196
3197 1169 Vandenberghe, J. (2003). Climate forcing of fluvial system development: an evolution
3198 of ideas. Quaternary Science Reviews, 22, 2053-2060.
3199 1170
3200
3201
3202
3203 1171 Vandenberghe, J. and Maddy, D. (2001). The response of river systems to climate
3204 change. Quaternary International, 79, 1-3.
3205 1172
3206
3207
3208 1173 Vergés, J., Marzo, M., Santaetulària, T., Serra-Kiel, J., Burbank, D. W., Muñoz, J. A. and
3209 Giménez-Montsant, J. (1998). Quantified vertical motions and tectonic evolution of the
3210 SE Pyrenean foreland basin. In: Masclé, A., Puigdefàbregas, C., Luterbacher, H.P. and
3211 1174
3212
3213 1175
3214
3215 1176
3216
3217 1177
3218
3219
3220
3221 1178
3222
3223 1179
3224
3225 1180
3226
3227
3228 1181
3229
3230
3231 1182
3232
3233
3234 1183
3235
3236 1184
3237
3238
3239 1185
3240
3241 1186
3242
3243
3244
3245

3246
3247
3248
1187 Wegmann, K.W. and Pazzaglia, F.J. (2009). Late Quaternary fluvial terraces of the
3249
3250
1188 Romagna and Marche Apennines, Italy: Climatic, lithologic, and tectonic controls on
3251
3252
3253
1189 terrace genesis in an active orogen. *Quaternary Science Reviews*, 28, 137-165.
3254
3255
3256
1190 Westaway, R., Bridgland, D.R., Sinha, R. and Demir, T. (2009). Fluvial sequences as
3257
3258
1191 evidence for landscape and climatic evolution in the Late Cenozoic: a synthesis of data
3259
3260
1192 from IGCP 518. *Global and Planetary Change*, 68, 237-253.
3261
3262
3263
3264
1193 Whipple, K. and Tucker, G. (1999). Dynamics of the stream-power river incision model:
3265
3266
1194 Implications for height limits of mountain ranges, landscape response timescales, and
3267
3268
1195 research needs. *Journal of Geophysical Research*, 104, 17661-17674.
3269
3270
3271
3272
1196 Whipple, K.X., Kirby, E. and Brocklehurst, S.H. (1999). Geomorphic limits to climate-
3273
3274
1197 induced increases in topographic relief. *Nature*, 401, 39-43.
3275
3276
3277
1198 Whitfield, R.G., Macklin, M.G., Brewer, P.A., Lang, A., Mau, B. and Whitfield (née
3278
3279
1199 Maher), E. (2013). The nature, timing and controls of the Quaternary development of
3280
3281
1200 the Rio Bergantes, Ebro basin, northeast Spain. *Geomorphology*, 196, 106-121.
3282
3283
3284
3285
1201 Willet, S.D., Hovius, N., Brandon, M.T. and Fischer, D.M. (2006). Introduction. In Willet,
3286
3287
1202 S.D., Hovius, N., Brandon, M.T. and Fischer, D.M. (eds.). *Tectonic, climate and*
3288
3289
1203 *landscape evolution*. The Geological Society of America, 398, vii-xi.
3290
3291
3292
3293
1204 Yang, G., Zhang, X., Tina, M., Brierley, G., Chen, A., Ping, Y., Ge, Z., Ni, Z. and Yang, Z.
3294
3295
1205 (2011). Alluvial terrace systems in Zhangjiajie of northwest Hunan, China: Implications
3296
3297
1206 for climate change, tectonic uplift and geomorphic evolution. *Quaternary*
3298
3299
1207 *International*, 233, 27-39.
3300
3301
3302
3303
3304

3305
3306
3307
3308
3309
3310
3311
3312
3313
3314
3315
3316
3317
3318
3319
3320
3321
3322
3323
3324
3325
3326
3327
3328
3329
3330
3331
3332
3333
3334
3335
3336
3337
3338
3339
3340
3341
3342
3343
3344
3345
3346
3347
3348
3349
3350
3351
3352
3353
3354
3355
3356
3357
3358
3359
3360
3361
3362
3363

1208 Zaprowski, B.J., Pazzaglia, F.J. and Evenson, E.B. (2005). Climatic influences on profile
1209 concavity and river incision. *Journal of Geophysical Research*, 110, F03004,
doi:10.1029/2004JF000138.

1211 Zeyen, H. and Fernández, M. (1994). Integrated lithospheric modeling combining
1212 thermal, gravity, and local isostasy analysis: application to the NE Spanish Geotransect.
1213 *Journal of Geophysical Research*, 99, 18089-18102.

Figure captions

1215 Figure 1. Location of the Cinca River drainage basin and the Ebro Basin in NE Iberia.

1216 Figure 2. Geological setting of the Cinca River Valley in NE Iberia (A) and geological
1217 mapping of the bedrock (adapted from Barnolas et al., 2009) (B).

1218 Figure 3. Distribution of terraces along the Cinca River valley (A). Detailed
1219 geomorphological maps and cross-sections of terraces in the Ainsa (B) and Albalate (C)
1220 sectors.

1221 Figure 4. Field photographs of terraces in the Cinca River valley: alluvial cover of the
1222 terrace Qt7 overlaying Eocene marls near Ainsa (A) and Miocene clays and sandstones
1223 near Almodáfar (B); deposits of terrace Qt7 made of massive and cross-stratified
1224 gravels near Albalate (C); preserved staircase terrace sequences in the Ainsa (D),
1225 Monzón (E) and Binaced (F) sectors.

1226 Figure 5. Grain size trends for Cinca River terrace deposits (Qt3, Qt7, Qt9) decreasing
1227 downstream.

3364
3365
3366
1228 Figure 6. Longitudinal profiles of the Cinca River terraces and the active channel.
3367

3368
1229 General parallel profiles with a subtle trend to divergence upstream are observed.
3369

3370
3371
3372
1230 Figure 7. Paleomagnetic analysis. Natural remanent magnetisation of the Cinca
3373

3374
1231 Terraces (A), orthogonal demagnetisation diagrams of selected samples (B) and
3375
3376
1232 paleomagnetic means values in the studied terraces (C).
3377

3378
3379
3380
1233 Figure 8. Fluvial incision rates in the Cinca River valley from successive preserved strath
3381

3382
1234 terraces at the upper reach (Ainsa sector) and at the lower reach (Albalate sector) of
3383

3384
1235 the valley. Spatial and temporal differences are clearly identified. Paleomagnetic
3385

3386
1236 timescale and marine isotope stages (adapted from Gibbard and Cohen, 2008) are
3387

3388
3389
1237 included.
3390

3391
3392
1238 **Table captions**
3393

3394
3395
1239 Table 1. Terraces, numerical dates and heights at the Albalate and Ainsa sectors of the
3396
3397
1240 Cinca River valley.
3398

3399
3400
3401
1241 Table 2. Summary of relative degrees of soil development on the Cinca River terrace
3402
3403
1242 surfaces and estimated ages.
3404

3405
3406
1243 Table 3. OSL dates from terraces in the the Cinca River valley (adapted from Lewis et
3407
3408
1244 al., 2009).
3409

3410
3411
3412
1245 Table 4. Paleomagnetic data. Location and UTM coordinates (T30). n/N;
3413

3414
1246 considered/analysed samples. Pol: Polarity. Dec/inc: magnetic declination and
3415

3416
1247 inclination and the Fisher (1954) statistical parameters (a_{95} and K).
3417
3418
3419
3420
3421
3422

3423
3424
3425
3426
3427
3428
3429
3430
3431
3432
3433
3434
3435
3436
3437
3438
3439
3440
3441
3442
3443
3444
3445
3446
3447
3448
3449
3450
3451
3452
3453
3454
3455
3456
3457
3458
3459
3460
3461
3462
3463
3464
3465
3466
3467
3468
3469
3470
3471
3472
3473
3474
3475
3476
3477
3478
3479
3480
3481

Table 5. Fluvial incision rates calculated from coupled preserved terraces in the Cinca River valley. Comparison of incision rates at the Ainsa and Albalate sectors is established. Temporal variations of incision rates at the Albalate sector are also evidenced.

Appendix captions

Appendix 1. Detailed geological map (including strath terraces) of the Cinca River valley. GPS measurements of elevation of terrace straths and active channel points are also indicated.

Appendix 2. Cinca River terrace strath data measurements and observations. UTM coordinates (latitude and longitude), elevation, substrate lithology (abbreviations: gyp, gypsum; ls, limestone; sst, sandstone), alluvium thickness (m), maximum grain size (Dmax), location and distance from headwaters are indicated. UTM coordinates and strath heights were obtained from a differentially corrected GPS accurate to 1 cm. Measurements from the headwaters of the river were obtained from topographic maps 1:25,000 in scale.

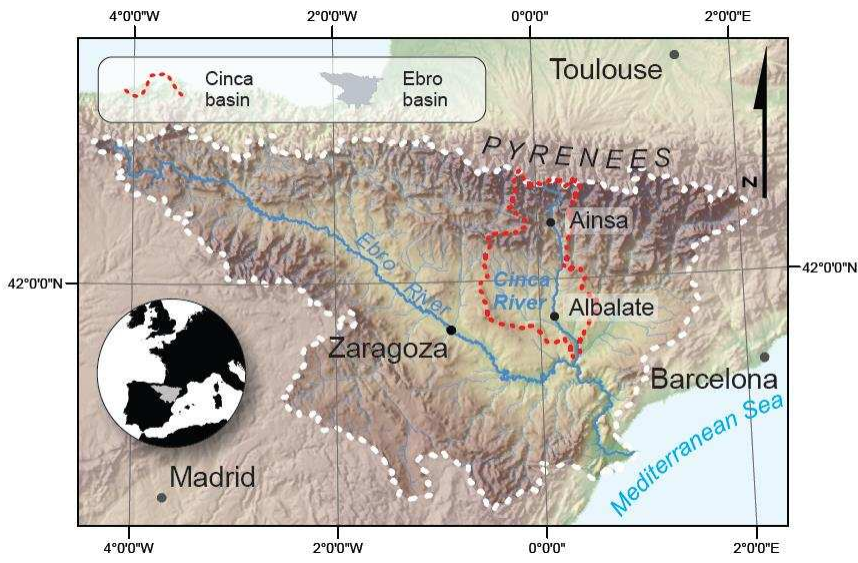


Fig. 1

Fig. 2

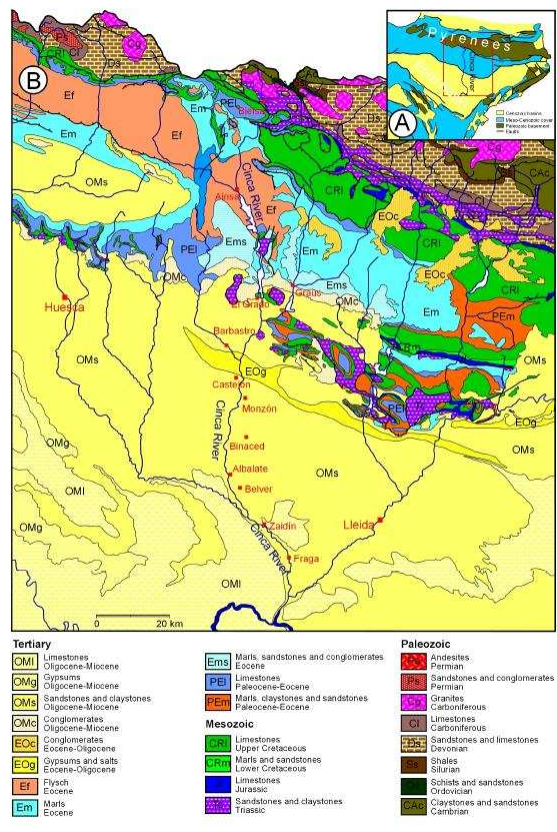


Fig. 3

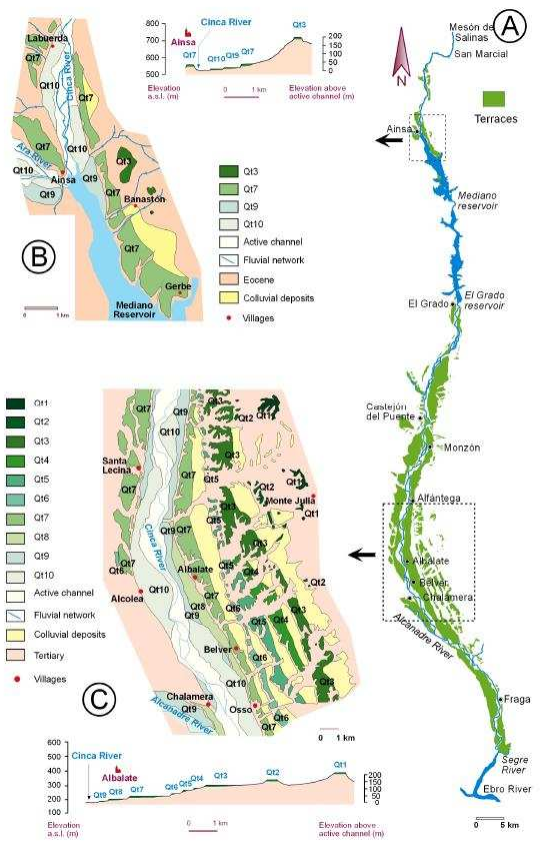


Fig. 2

Fig. 3

Fig. 4

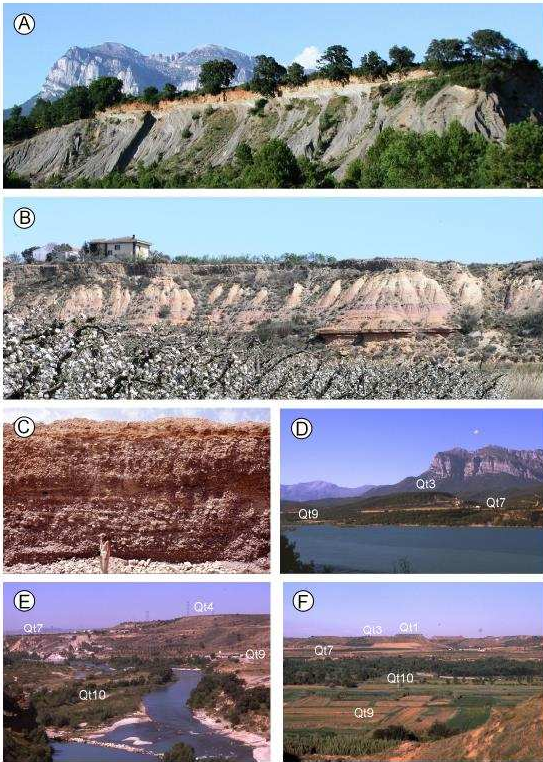


Fig. 7 below

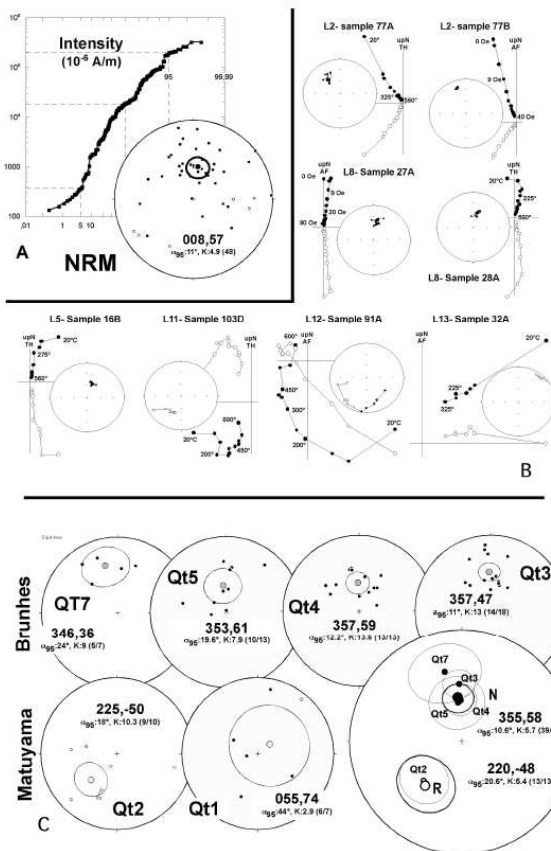


Fig. 5

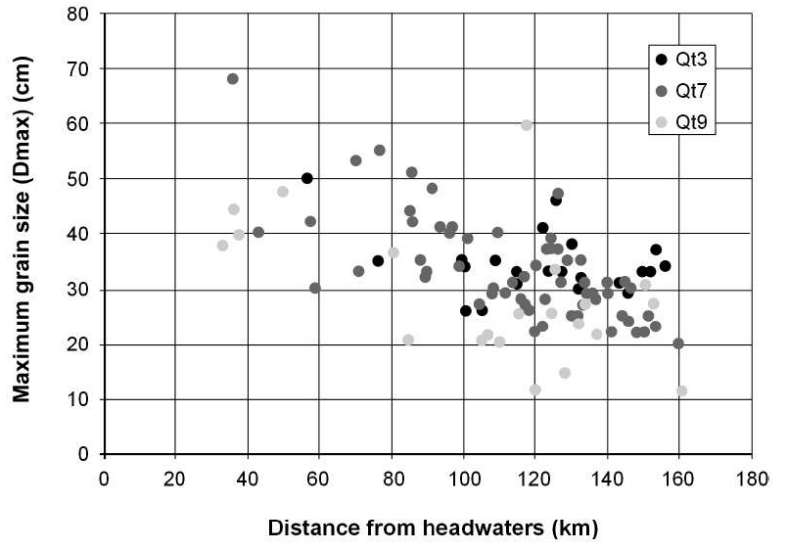


Fig. 6

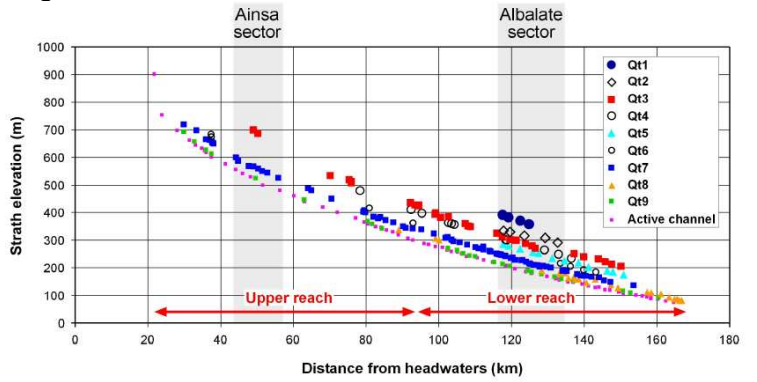
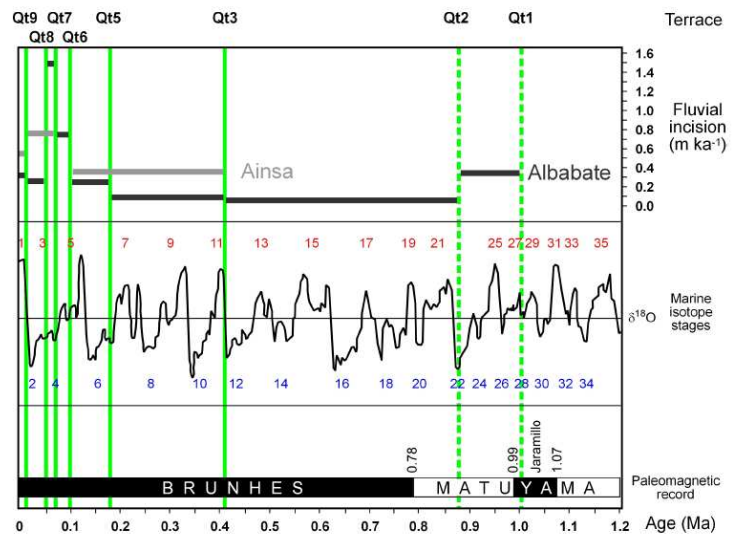
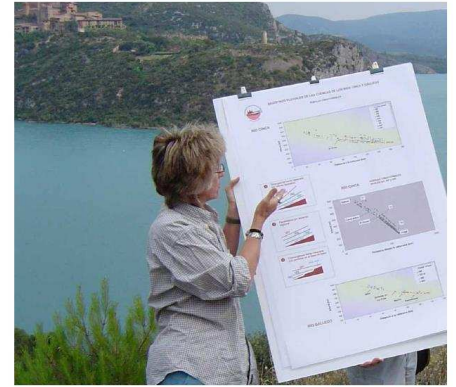


Fig. 8



Appendix 1



LEGEND

	Tertiary		Quaternary
	Miocene		Fluvial terraces
	Conglomerates		Q11
	Sandstones and shales		Q12
	Limestones and marls		Q13
	Oligocene		Q14
	Sandstones and shales		Q15
	Conglomerates		Q16
	Sandstones, shales and conglomerates		Q17
	Shale and sandstones		Q18
	Sandstones, shales and conglomerates		Q19
	Marls and limestones		Q20
	Eocene		Active channel
	Limestones with shales		Colubines
	Limestones and marls		Monines
	Blue marls		
	Turbidites		
	Sandstones, shales and conglomerates		Other information
	Sandstones		Arches
	Sandstones and conglomerates		Synclines
	Paleocene		Faults
	Limestones and dolomites		Fluvial network
	Shale, sandstones and limestones (clay-rich)		Roads
	Mesozoic		Rivers
	Cretaceous		Death elevations (DPE)
	Limestones		
	Sandstones		
	Limestones and dolomites		
	Tertiary		
	Shale, gypsum and dolomites		
	Sandstones and conglomerates		
	Chalks		
	Paleozoic		
	Carboniferous		
	Shale and limestones		
	Devonian		
	Quartzites		
	Slates		
	Limestones		
	Gneisses		

Table 1. Terraces, numerical dates and heights at the Albalate and Ainsa sectors of the Cinca River valley.

Terrace	Age (Ky)	Height (m)	
		Ainsa sector	Albalate sector
Qt1	999-1070 ^c	-	182.1
Qt2	780-999 ^c	-	132.5
Qt3	401±117 ^b	172.5	103.5
Qt4	-	-	91.3
Qt5	178 ± 21 ^a	-	79.9
Qt6	97±16 ^a	-	60.4
Qt7	61 ± 4 ^a	44.2	33.9
Qt8	47 ± 4 ^a	-	13.1
Qt9	11 ± 1 ^a	6.0	3.6

^a Numerical age from Optical Stimulated Luminescence (Lewis et al., 2009)
^b Age derived from soil chronofunction used in Lewis et al. (2009)
^c Tentative age from paleomagnetic data

Table 2. Summary of relative degrees of soil development on the Cinca River terrace surfaces and estimated ages.

Terrace	PDI Value Range (number of soils) ¹	Soil Age ²	Source of Age ³	MAX B Horizon Type ⁴	MAX Carbonate Stage Morphology ⁵
Albalate Sector					
Qt9	14.7-18.1 (2)	11±1	OSL	Bk-Bwk	I+
Qt8	23.2-24.7 (2)	47±4	OSL	Bk-Btk	I-II
Qt7	27.0-33.3 (5)	61±4	OSL	Btk-Bkm	II-III
Qt6	43.2 (1)	97±16	OSL	Btk	III+
Qt5	45.1-59.9 (3)	178±21	OSL	Bk-Bkm	III+-IV+
Qt3 ⁶	61.4-80.6 (5)	401±117	PDI	Bt-Bk-Bkm	IV-V+
Ainsa Sector					
Qt9	39.3 (1)	11±1	OSL	Btk	I
Qt7	64.4-67.9 (2)	61±4	OSL	Bt-Btk	I
Qt3	105.1 (1)	-	-	Bt	none

¹ Profile Development Index value and number of soils described shown in (). Minimum and maximum PDI values show when more than 2 soils
² Age of soil on terrace surface
³ OSL: Optical Stimulated Luminescence, PDI: age derived from soil chronofunction used in Lewis et al (2009)
⁴ Strongest, best develop B horizon type in each soil profiles. Subscripts shown are w: color or structure B, k: accumulation of carbonates; t: accumulation of clay; m: cemented
⁵ Carbonate stage morphology from Gile et al. (1981) and Birkeland (1999)
⁶ PDI values for the 5 Qt3 soils near Albalate are 61.4, 75.1, 64.9, 64.8, 80.8, respectively

Table 3. OSL dates from terraces in the Cinca River valley (adapted from Lewis et al., 2009).

Lab Code	Terrace	Northing	Easting	De (Gy)	Dose rate (mGy/a)	OSL date (ka)
X398	Qt5	4618380	266866	237±26	1.39±0.09	171±22
X399	Qt5	4619473	266357	209±7	1.16±0.7	180±12
X397	Qt6	4618085	266253	157±23	1.62±0.11	97±16
X396	Qt7	4700762	265624	156±26	2.46±0.18	63±12
X1122	Qt7	4700762	265624	128±27	2.16±0.12	59±13
X823	Qt7	4678877	270913	82±15	1.28±0.08	64±13
X197	Qt7	4618846	265647	150±3	2.45±0.12	61±3
X199	Qt7	4613809	267775	101±5	1.80±0.09	56±4
X198	Qt7	4613809	267775	118±5	1.62±0.10	65±5
X817	Qt8	4624970	262087	89.0±10.2	2.26±0.14	39±5
X821	Qt8	4614698	267127	83±10	1.96±0.13	42±6
X833	Qt8	4598786	279236	117±6	2.50±0.16	47±4
X808	Qt8	4598765	278848	88±4	1.75±0.10	50±4
X809	Qt8	4598765	278848	90±2	1.79±0.11	50±3
X828	Qt9	270671	270671	18.3±1.1	1.86±0.12	10±1
X826	Qt9	266149	266149	21.8±0.7	1.89±0.13	12±1
X812	Qt9	266149	266149	18.0±7.6	1.46±0.07	9±4
X813	Qt9	266149	266149	27.0±3.6	1.91±0.10	14±2
X816	Qt9	261783	261783	26.5±1.8	2.15±0.14	12±1
X806	Qt9	263612	263612	23.0±2.3	2.03±0.11	11±1
X807	Qt9	263612	263612	22±1.4	1.96±0.10	11±1
X832	Qt9	275009	275009	18.4±3.6	1.81±0.12	10±2

Table 4
Paleomagnetic data. Location and UTM coordinates (T30), n/N; considered/analyzed samples. Pol: Polarity. Dec/inc: magnetic declination and inclination and the Fisher (1953) statistical parameters (a95 and K).

Terrace	Pit	X (30T)	Y (30T)	Locality	Samples	n	N	Dec	Inc	a95	K	Pol				
Qt7	TA2-1	759,286	4,700,351	Ainsa (Polideportivo)	P85 to P90	3	3	329	32	26.7	33.6	N				
	TA4-1	760,468	4,698,252	Banastón (Caballos)	P77 to P84	2	4	13	38	32.0	125.7	N				
					PCA only	5	7	346	36	24.0	9.0	N				
Qt5	T6-1	766,285	4,619,535	Belver (Plana Valentina)	P01 to P09	6	8	354	64	21.5	12.8	N				
	T6-1	765,701	4,620,590	Belver (Granja Baillarín)	P10 to P15	4	5	350	56	54.3	5.1	N				
Qt4	T7-1	766,023	4,622,346	Belver (Los Almendros)	P16 & P17	2	4	22	49	37.1	94.8	N				
					T7-3	767,682	4,620,960	Belver (Silvio Ballarín)	P44 to P54	3	3	288	55	24.6	10.0	N
									PCA + demagnetization circles	13	13	357	59	12.2	13.6	N
Qt3	T8-1	764,028	4,628,305	Albalate (Los Olivos)	P18 to P24	4	4	26	25	49.7	5.9	N				
	T8-2	763,799	4,627,424	Albalate (El Chopo)	blocks P25 to P28	10	11	5	51	12.0	18.9	N				
	T8-4	764,028	4,628,305	Albalate (Las Lecineras)	P107 to P110	3	3	339	35	31.3	24.9	N				
Qt2	T9-1	765,203	4,629,205	Albalate (Mombrun)	PCA only	14	18	357	47	11.0	13.0	N				
					P55 to P57 + P68 to P70	3	3	153	-71	87.3	4.6	R				
					P103 to P106	4	4	203	-41	5.7	351.1	R				
Qt1	T9-2	765,126	4,628,812	Albalate (Mombrun)	P91 to P102	3	3	275	-37	22.9	11.4	R				
	T9-3	765,200	4,628,537	Albalate (Mombrun)	PCA + demagnetization circles	9	10	225	-50	18.0	10.3	R				
Qt1	T10-2	767,495	4,629,475	Albalate (San Salvador)	P29 to P34	6	7	55	74	44.0	2.9	N				
	Cinca Terraces-Reverse					10	10	220	-48	20.6	5.4	R				
	Cinca Terraces-Normal					48	58	355	58	10.6	5.7	N				
	Cinca Terraces-N + R					58	68	8	57	9.8	5.1	N + R				

Table 5
Fluvial incision rates calculated from coupled preserved terraces in the Cinca River valley. Comparison of incision rates at the Ainsa and Albalate sectors is established. Temporal variations of incision rates at the Albalate sector are also evidenced.

Coupled terrace	Differential incision (m)	Elapsed time (Ka)			Incision rate (m/ky)		
		Mean	Minimum	Maximum	Mean	Minimum	Maximum
Qt3-Qt7 Ainsa	128.3	340	219	461	0.38	0.59	0.28
Qt3-Qt7 Albalate	69.6	340	219	461	0.20	0.32	0.15
Qt7-Qt9 Ainsa	38.2	50	45	55	0.76	0.85	0.69
Qt7-Qt9 Albalate	30.3	50	45	55	0.61	0.67	0.55
Qt9-Active channel Ainsa	6.0	11	10	12	0.54	0.6	0.5
Qt9-Active channel Albalate	3.6	11	10	12	0.33	0.36	0.3
Qt1-Qt2 Albalate	49.6	145 ^a	no	no	0.34 ^a	no	no
Qt2-Qt3 Albalate	29.0	488 ^a	no	no	0.06 ^a	no	no
Qt3-Qt5 Albalate	23.6	223	85	361	0.11	0.28	0.07
Qt5-Qt6 Albalate	19.5	81	66	108	0.24	0.29	0.18
Qt6-Qt7 Albalate	26.5	36	26	46	0.74	1.02	0.58
Qt7-Qt8 Albalate	20.8	14	22	6	1.48	0.94	3.45
Qt8-Qt9 Albalate	9.5	36	41	31	0.26	0.23	0.31
Qt9-Active channel Albalate	3.6	11	10	12	0.33	0.36	0.30

^a Indicative data.

Y (m)	X (m)	Strath elevation (m)	Substrate	Max. rep. grain size (cm)	Location	Distance from headwaters (km)
Qt1 strath						
4626238,7	268814,2	357,31	sst, clay	48	Monte Julia	130,40
4628762,5	268160,6	369,94	clay, sst	48	San Salvador	128,00
4631710,0	266994,0	382,77	clay, sst	43	Brujas	124,70
4633561,1	266598,0	391,65	clay, sst	30	Binaced, pine	123,10
				mean = 42 ± 9		
Qt2 strath						
4622779,0	269090,4	291,86	clay	40	Belver	138,20
4626128,2	267180,0	307,69	sst	42		134,80
4627915,5	266335,7	316,46	clay, sst	48	Mombrun	129,05
4631605,1	265448,4	329,24	clay	36	Binaced 2	125,15
4633506,8	265338,9	333,99	clay, sst	39	Binaced 1	123,35
				mean = 41 ± 4		
Qt3 strath						
4606834,7	275456,5	204,54	clay	34	Zaidin south	155,65
4609076,4	274022,9	212,25	clay	37	Zaidin	153,10
4610459,5	272542,3	221,32	clay	33	San Anton	151,30
4612664,1	272105,5	231,46	ls, clay	33	Zaidin north, peaches	149,45
4615680,8	270893,7	239,25	clay	29	Almudafar	145,45
4617633,2	269497,0	251,03	clay	31	Osso	142,79
4624783,7	265615,0	269,81	clay	32	Albalate, Porquet	132,10
4625718,6	264849,8	278,70	sst	30	Lecineras south	131,25
4627553,2	264705,4	287,57	clay, sst	38	Lecineras north	129,45
4629600,5	264481,2	299,33	clay	33	Las Brujas west	126,85
4630292,1	264604,0	300,16	clay	33	Las Brujas west	126,60
4631856,3	263793,9	302,45	clay	46	Alfantega-Albalate	125,15
4633829,1	264075,3	312,84	sl, sst	33	Alfantega south	123,05
4635456,3	264683,0	324,76	sst, clay	41	Alfantega north	121,60
4641433,4	267164,4	348,76	sst	33	Monzon south	114,30
4642139,0	267230,3	351,28	clay	31	Monzon, cemetery	113,60
4643345,2	267354,5	359,67	clay	NA	Monzon, castle	112,80
4648994,7	264935,1	384,64	sst clay	35	Castejon, gravel pit	108,20
4650942,7	264077,2	382,30	gyp	NA	Castejon-Salinas	106,10
4651648,2	264273,7	398,07	gyp	NA	Castejon	104,70
4652887,4	269341,9	393,82	clay	26	Fonz 3	104,55

4656953,7	265155,5	427,86	sst, clay	26	Las Coronas 3	100,05
4657059,2	265420,3	424,30	clay, sst	34	Las Coronas 1	99,95
4657890,1	265794,1	427,42	clay, sst	35	Las Coronas 4	98,95
4659224,5	266451,3	435,14	cgl, sst	NA	Las Coronas 2	97,80
4673397,6	270716,4	507,73	cgl	NA	Torreciudad 2	81,55
4673470,8	270762,6	511,44	cgl, clay	NA	Torreciudad	81,55
4674106,1	270586,2	519,12	clay	NA	Torreciudad north	80,90
4679386,0	270652,0	533,57	clay	35	Abizanda-Moscarazos	75,70
4698766,8	267451,0	687,52	sst, marls	50	Santa Tecla	55,80
4698820,7	267324,8	685,63	marls	NA	Santa Tecla	55,80
4699527,8	267293,3	698,75	marls, sst	NA	Arnal	54,55

mean = 34 ± 6

Qt4 strath

4618310,2	268999,2	234,51	clay	41	Osso	142,00
4621360,8	267202,7	249,02	clay	27	Belver	138,50
4623856,0	265718,1	264,08	clay	31	Albalate	134,65
4632761,8	263831,0	299,94	clay, sst	41	Alfaltega south	124,20
4633014,6	263912,7	301,32	cl	43	Binaced road	123,95
4647516,3	264286,8	356,10	clay, sst	26	Castejon, horse arena	109,85
4648272,3	264594,9	360,26	sst, clay, gyp	NA	Castejon 1	109,05
4648923,5	265099,9	363,73	sst	NA	Castejon, gravel pit	108,20
4654312,1	269983,2	397,45	clay	NA	Fonz 1	100,95
4657383,2	270205,3	410,16	clays	NA	Fonz 2	97,95
4671239,3	271297,4	478,68	cgl, sst, clays	NA	El Grado	83,90

mean = 35 ± 8

Qt5 strath

4604667,1	276619,5	175,11	clay, sst, lm	28	Pilaret-Fraga 1	158,35
4606841,1	275133,3	185,07	clay, marls	36	Zaidin south	155,45
4608012,4	273923,2	189,64	clay	NA	Zaidin	153,85
4612314,6	270700,4	202,56	clay, sst	39	Zaidin	148,70
4615106,6	269791,6	219,61	clay	51	Almudafar	146,00
4617641,2	268022,3	226,21	clay	29	Osso	142,10
4620596,2	266439,1	235,60	clay	38	Belver	138,70
4623348,5	264910,9	254,56	clay, sst	46	Albalate	134,90
4625398,1	264561,8	257,27	clay	NA	Lecineras	131,50
4627116,2	264081,3	268,53	clay	37	Clamor	129,90
4629659,3	263752,5	279,92	clay	37	Alfantega-Albalate 2	126,75
4631764,0	263530,5	285,61	sst, clay	41	Alfantega-Albalate 1	125,30

mean = 38 ± 7

Qt6 strath

4612095,2	270574,9	184,55	clay	31	Zaidin	148,80
4614561,5	268279,5	192,57	clay	24	Almudafar	145,40
4617395,8	266899,7	205,17	clay	38	Osso	141,75
4619988,9	265939,2	215,59	clay, sst	46	Belver	139,00
4662716,8	271705,9	362,57	sst, marls	30	Estada	98,45
4668560,4	272171,0	416,16	sst	27	Artasona	86,45
4710107,9	264958,2	673,64	not seen	80	Laspuna	43,05
4710475,2	265867,2	683,96	marls	NA	Laspuna	42,90

mean = 39 ± 19

Qt7 strath

4603962,4	276944,5	136,17	clay, silt	20	Pilaret	159,15
4608542,3	272710,3	148,99	ls	23	Zaidin south	152,80
4609939,6	271780,7	154,18	ls, clays	25	Zaidin	151,00
4611129,6	270605,8	165,74	clay, ls	22	Ave	149,60
4612328,1	269279,9	167,12	clay	22	Almudafar south	147,55
4613510,6	268000,6	171,28	clay	30	Almudafar south 2	145,95
4613818,8	267774,6	170,83	sst?	24	Almudafar, gravel pit	145,55
4614506,9	267304,1	172,25	sst, clay	31	Almudafar north	144,65
4615711,5	266825,8	177,04	ls, clay	25	Osso south	143,60
4617975,1	266027,5	188,40	cl?	22	Osso north	140,75
4618821,2	265551,1	190,81	sst, ls, clay	29	Belver, Tejerias	139,75
4619145,8	265392,6	189,07	clay	31	Belver	139,65
4621596,7	264063,9	199,87	sst, silt	28	Albalate	136,35
4621619,2	264052,5	199,71	sst, silt	NA	Albalate	136,35
4622728,3	263753,3	204,00	silt, sst	29	Albalate	135,20
4623531,0	263013,5	207,42	clay, sst	29	Albalate	134,20
4623528,9	259973,4	203,89	silt, clay	31	Alcolea	133,25
4625094,6	259311,4	209,43	clay	27	Alcolea north	132,74
4624817,7	262567,7	208,95	clay	35	Albalate km 1	132,30
4625514,2	259383,6	209,85	clay	NA	Alcolea north 2	131,65
4626568,0	259527,9	213,21	clay?	25	Santa Lecina, Viruelas	130,70
4626521,5	262161,2	216,06	clay, sst	25	Albalate km 3	130,45
4629220,0	260490,3	222,01	sst	25	Santa Lecina south	129,60
4628634,8	262493,1	228,18	sst, clay	NA	Albalate km 5.5	128,60
4628801,0	262431,0	226,97	clay	NA	Albalate km 6	128,30
4628801,1	262430,8	227,67	clay	35	Albalate km 6	128,30
4630222,5	260538,4	228,20	clay	31	Santa Lecina north	126,60
4631295,0	262957,6	235,87	sst, clay	47	Albalate km 8	125,85

4631388,9	263081,3	237,28	sst	37	Albalate km 8	125,85
4631924,0	260920,1	234,55	st, clay	NA	Estiche south	125,45
4633048,6	263181,9	241,37	clays	37	Binaced road	123,95
4633660,7	260901,2	242,52	clay, sst	39	Estiche	123,80
4634429,6	263302,9	246,29	clay	37	Alfantega south	122,77
4635076,2	263518,3	248,91	clay	28	Alfantega	122,45
4635076,0	263519,1	248,84	clay	NA	Alfantega	122,05
4635999,8	261450,7	250,32	clay, sst	23	Estiche north	121,50
4637344,9	263780,0	258,93	sst, clay	34	Pueyo	119,85
4637984,2	261620,5	261,21	clay	22	Pomar north	119,50
4639441,3	264658,1	269,06	sst, clay	NA	Pueyo	117,80
4639697,2	262563,3	265,73	clay, sst	NA	Conchel south 2	117,80
4639713,5	262565,1	276,29	clay, sst	26	Conchel south 2	117,80
4640762,0	263112,8	269,41	sst, clay	27	Conchel	116,65
4640326,8	264903,1	270,19	clay, sst	32	Alegria	116,55
4641521,3	263719,4	274,05	sst	28	Conchel north	115,65
4643649,4	264741,5	283,85	sst	31	Selgua	113,35
4645806,7	265061,4	292,63	clay, sst	29	Monzon north	111,25
4647577,6	265271,7	295,37	sst, clay	NA	Castejon, concrete plant	109,55
4647937,3	265274,5	302,00	sst	NA	Castejon (repeat)	109,05
4647937,5	265275,1	302,98	sst, clay	40	Castejon	109,05
4648783,4	266670,7	310,82	not seen	NA	Chula Vista	107,95
4648737,8	266624,3	309,66	sst, clay	NA	Chula Vista	107,95
4648783,4	266670,7	310,82	sst, clay	30	Chula Vista	107,95
4649518,1	267381,8	307,92	gyp	29	Ariestolas	107,45
4653028,9	268364,0	324,47	clay?	27	Cofita	104,15
4655141,4	267896,4	338,23	sst	39	Fonz	100,80
4657703,6	267937,3	341,73	sst, cgl, clay	34	Arias II	98,40
4658881,1	268853,8	344,51	cgl	41	Casa Pararayos	96,50
4659779,8	269184,5	349,60	sst	40	Central Electrica Pilas	95,70
4662686,0	269983,7	364,44	clay, sst	41	Enate	93,10
4664323,9	270860,5	372,14	clay, sst	48	Enate north	90,90
4665668,4	271111,9	383,23	cgl, sst	33	El Grado south	89,45
4666272,9	271795,1	378,93	sst, cgl	32	Olvena	88,90
4667415,4	271756,1	385,12	sst, cgl	35	Artasona south	87,60
4669740,5	270777,3	400,65	clay	42	El Grado	85,35
4670069,9	271665,4	408,35	sst	51	El Grado dam 2	85,05
4670299,3	271420,3	402,16	ls	44	Dam	84,75
4678793,0	270908,2	449,57	marls?	55	Moscarazos	76,05
4684220,2	270139,2	479,93	ls, marls	33	Liguierre	70,50

4685135,5	270156,0	488,43	Triassic red beds	53	Liguerre2	69,60
4692888,6	268198,3	525,39	marls	NA	Ainsa, airport	61,40
4696062,9	267620,1	543,96	marls	30	Gerbe	58,45
4697188,3	266541,9	550,44	sst, marls	42	Banaston	57,00
4698268,3	266398,0	559,25	marls	NA	Banaston 2	55,85
4699552,2	266071,0	566,39	sst	NA	Usana	54,55
4700761,5	265623,9	568,12	marls	NA	Pueyo-Ainsa	53,30
4703367,9	265076,6	587,06	marls	NA	Ainsa north	50,40
4703968,8	264325,4	599,71	marls	NA	Labuerda	49,80
4709582,2	265366,6	650,20	marls	NA	Escalona	43,60
4709906,5	265387,2	653,19	marls	NA	Escalona2	43,25
4709912,6	265032,2	655,82	marls	NA	Escuain hwy	43,20
4710744,3	265700,3	662,57	marls	40	Laspuna	42,55
4711889,9	265799,1	664,36	marls	NA	Laspuna north	41,45
4714062,0	266742,2	697,85	ls	NA	Misuellas	38,90
4713888,6	269696,5	718,61	marls	68	Badiain	35,40

33 ±9

Qt8 strath

4590370,1	279052,3	80,17	ls	NA	Escarpe, convent	172,40
4590370,5	279052,6	80,24	ls	NA	Escarpe, convent	172,40
4590891,4	279123,9	80,10	ls	25	Masalcorreig	171,80
4590945,9	279117,4	81,53	ls	NA	Masalcorreig	171,80
4591745,5	279254,7	86,95	ls	NA	Masalcorreig	171,05
4592329,1	279302,0	85,93	marls, ls	23	Masalcorreig south	170,35
4593975,4	279633,5	91,86	sst, clay	27	Masalcorreig north	168,85
4597707,6	279414,7	105,00	clay,sst	NA	Fraga south	166,65
4598786,9	279212,5	108,89	clay,sst	NA	Fraga hwy work	163,95
4599957,9	278910,1	111,15	sst, clay	NA	Fraga	162,90
4606658,0	274037,9	125,52	clay, sst, ls	NA	Clamor, confluence	154,85
4607369,5	271680,2	137,35	clay	28	Velilla	152,90
4610224,5	268472,5	158,00	clay	25	Velilla, Ave	148,55
4612890,9	267490,8	145,63	clay	31	Almudafar south	146,15
4615161,1	266942,4	158,30	clay, sst	25	Almudafar north	144,05
4614753,1	265034,6	157,11	clay, marls	25	Chalamera-Ballobar	143,10
4616088,7	266511,0	166,68	clay	NA	Osso	142,65
4617565,5	265856,2	162,10	clay	35	Osso north	141,15
4617332,9	263643,4	180,52	clay	42	Chalamera	140,15
4618685,0	262929,1	179,86	clay	36	Chalamera, hermitage	138,75
4624667,5	262009,9	188,57	?	22	Albalate	133,90
4651338,4	267816,2	299,06	gyp	28	Cofita south	105,65

4652421,1	267841,3	305,88	gyp, marls	27	Cofita, canal	104,65
4660668,2	269984,0	336,43	Keuper facies	NA	Estadilla	94,50
				mean = 29 ± 6		
Qt9 strath						
4596667,0	279164,7	93,79	clay, sst	12	Fraga toll rd	160,45
4603299,3	275311,1	101,25	sst, clay	28	Miralsot south	152,75
4605605,7	275012,0	116,38	sst, clay	31	Zaidin south, gravel pit	150,60
4615652,4	265127,9	152,28	clay?	22	Chalamera-Ballobar	136,95
4618197,2	263357,3	159,90	sst, clay	28	Chalamera, hermitage	133,70
4620341,8	264057,6	168,05	clay	24	Albalate-Belver	131,85
4623545,6	262027,5	177,68	?	15	Albalate	128,25
4626222,8	261433,0	184,79	sst	34	Las Torres	125,50
4627246,1	261894,9	190,18	sst	26	Ciguena	124,50
4632191,0	262278,6	205,64	sst	12	Soto del Tros north	119,40
4633967,1	262899,7	213,73	clay, sst	60	Alfantega	117,55
4636516,8	262991,4	220,84	cl	26	Pueyo	115,25
4641308,4	264711,2	241,67	sst	21	Alegria	110,00
4642910,2	265578,5	244,41	sst	NA	Monzon south	108,40
4644355,7	266152,6	251,55	sst, clay	22	Sosa confluence	106,70
4646366,6	265770,4	263,05	sst	21	Monzon north	105,05
4648800,4	266119,5	267,70	sst	NA	Castejon 2	102,45
4648906,0	266183,6	271,11	sst	NA	Castejon 1	102,45
4665046,2	272113,9	341,86	not seen	21	Esera confluence	84,35
4667582,6	270679,9	358,33	not seen	NA	El Grado south	81,70
4669267,9	270600,1	369,16	not seen	37	El Grado south	80,40
4686475,7	270644,5	446,97	ls	NA	Liguerre, bridge	62,95
4698725,7	265976,7	524,26	marls (approx.)	48	Usana	49,60
4710107,5	265784,0	612,75	marls	40	Laspuna	37,50
4711924,7	265460,0	627,23	marls	45	Laspuna	35,90
4714416,3	266839,4	657,03	marls	38	Hospital de Tella	32,75
4714170,9	269863,3	692,99	ls, marls	NA	Lafortunada	29,90
				mean = 29 ± 12		
Active channel						
4590568,2	278243,3	76,16		NA	Torrente south	167,50
4592675,2	279204,4	74,58		NA	Masalcorreig	166,50
4594870,8	278388,8	79,66		NA	Torrente de Cinca	164,60
4596928,2	278849,5	86,71		NA	Fraga toll rd	162,50
4598806,7	278948,2	91,45		NA	Fraga	160,20
						158,35

4598821,9	278940,5	87,89		NA	Fraga circunvalacion	158,35
4600248,2	278725,2	94,51		NA	Fraga	157,25
4601693,1	278159,6	98,36		NA	Zaidin-Fraga 4	155,95
4603247,8	277358,1	101,14		NA	Zaidin-Fraga 3	154,25
4604209,4	276322,3	106,41		NA	Miralsot south	152,70
4605611,4	274968,5	105,92		NA	Zaidin south, gravel pit 2	150,75
4606472,3	274068,0	112,86	ls	NA	Zaidin-Fraga 2	149,55
4608479,0	272650,7	119,77		NA	Zaidin 1	147,05
4609465,8	271366,8	120,59	ls	NA	Zaidin	145,70
4610187,2	269704,0	129,27		NA	Ave south	144,05
4610378,3	268514,1	128,03		NA	Ballobar, Ave	143,00
4612062,3	267550,6	133,60		NA	Almudafar south	141,15
4613488,6	266644,3	140,72		NA	Almudafar	139,45
4615639,9	265193,2	147,30		NA	Chalamera-Ballobar	137,00
4616710,9	264612,4	148,82		NA	Chalamera	135,55
4618298,0	263415,2	155,20		NA	Chalamera, hermitage	133,20
4618566,0	263392,3	160,45		NA	Belver	133,40
4619667,1	263075,0	166,23		NA	Belver north	132,30
4620039,9	262992,4	159,69		NA	Albalate south	132,22
4622262,0	262463,6	169,12		NA	Albalate south	129,75
4623423,1	261865,3	176,13		NA	Albalate	128,30
4623430,2	261865,1	175,24		NA	Albalate	128,35
4626195,7	261399,3	180,14	sst	NA	Las Torres	125,50
4627618,6	261822,7	185,31	sst	NA	Ciguena	123,95
4630745,8	261361,0	196,13		NA	Soto del Tros	120,95
4633356,8	261767,0	207,86		NA	Estiche	118,35
4637273,7	262133,7	221,03		NA	Pomar	114,80
4639503,1	262665,8	228,24		NA	Pueyo	112,35
4640927,9	263980,0	235,68		NA	Conchel	110,60
4643437,3	265673,5	241,04		NA	Selgua-Monzon	107,60
4644809,6	265867,9	250,61		NA	Monzon	106,35
4646194,6	265594,6	257,47		NA	Monzon north	105,15
4648060,5	265631,7	258,81		NA	Castejon	103,40
4648969,3	266539,5	263,55		NA	Castejon 2	102,20
4650585,0	265670,5	273,82		NA	Castejon 3	101,05
4652004,2	265839,1	277,07		NA	Cofita	99,10
4653915,1	265547,3	285,08		NA	Vero confluence	97,20
4655130,7	266128,3	288,41		NA	Vero confluence north	96,00
4658190,6	266885,9	299,79	sst, cgl dipping 45N	NA	Arias II	92,85
4659504,4	267534,9	306,99		NA	Coronas north	91,50

4660935,1	269750,3	319,45	NA	Puente las Pilas	88,90
4662402,9	270235,1	329,67	NA	Enate 2	87,35
4663979,8	271147,6	336,60	NA	Enate	85,60
4665299,6	271386,7	346,06	NA	Piscifactoria	84,10
4666952,5	271084,7	349,10	NA	Artasona south	82,65
4669068,8	271402,9	358,94	NA	El Grado	80,50
4670028,2	271513,5	365,31	NA	El Grado dam	79,50
4672400,0	271300,0	380	NA		77,15
4677400,0	271000,0	400	NA		72,10
4681300,0	272500,0	420	NA		68,10
4686300,0	274000,0	440	NA		63,05
4889100,0	270000,0	460	NA		60,15
4692750,0	268750,0	480	NA		56,30
4696800,0	266450,0	500	NA		51,55
4699976,5	264920,2	528,59	NA	Ainsa	48,25
4702081,1	264805,0	541,17	NA	Ainsa north	46,05
4704007,1	264807,9	555,85	NA	Labuerda	44,15
4706553,1	265675,7	575,91	NA	Labuerda north	41,35
4710050,0	265753,7	601,17	NA	Laspuna, bridge	37,50
4711829,8	265405,3	617,64	NA	Laspuna north	36,00
4711989,0	265561,9	623,30	NA	Puertolas	35,60
4712750,6	266107,4	633,25	NA	Puertolas north	34,80
4713987,4	266833,0	644,17	NA	Misuellas	33,15
4714366,8	268440,4	661,44	NA	Laspuna reservoir	31,40
4715470,8	270601,9	697,83	NA	Devotas	28,05
		740	NA		25,70
4718416,4	270829,7	753,47	NA	Salinas	25,05
		780	NA		23,70
		800	NA		23,45
4720183,9	273539,0	900,84	NA	Bielsa south, gorge	21,70
4723000,2	272895,7	973,66	NA	Bielsa	18,65
4724306,0	271381,9	1087,65	NA	Javierre	16,45
4725075,8	268267,4	1161,20	NA	Pineta 2	12,95
4729158,6	261407,7	1273,24	NA	Pineta	5,25
		1300	NA		4,25
		1400	NA		3,75
		1500	NA		3,35
		1600	NA		2,95
		1700	NA		2,75
		2100	NA		2,25

2200	NA	2,10
2500	NA	1,25
2520	NA	0,75
2600	NA	0,25
2700	NA	0,03